

Coronal–Temporal Correlations in GX 339–4: Hysteresis, Possible Reflection Changes, and Implications for ADAFs

M.A. Nowak^{1,2}, J. Wilms³, J.B. Dove⁴

¹ *JILA, University of Colorado, Campus Box 440, Boulder, CO 80309-0440, U.S.A.;*

² *current address, MIT-CXC, NE80-6077, 77 Massachusetts Ave., Cambridge, MA 02139, U.S.A.*

³ *Institut für Astronomie und Astrophysik, Abt. Astronomie, Waldhäuser Str. 64, D-72076 Tübingen, Germany;*

⁴ *Dept. of Physics, Metropolitan State College of Denver, C.B. 69, P.O. Box 173362, Denver, CO 80217-3362, U.S.A.*

1 November 2018

ABSTRACT

We present spectral fits and timing analysis of Rossi X-ray Timing Explorer observations of GX 339–4. These observations were carried out over a span of more than two years and encompassed both the soft/high and hard/low states. Two observations were simultaneous with Advanced Satellite for Cosmology and Astrophysics observations. Hysteresis in the soft state/hard state transition is observed. The hard state exhibits a possible anti-correlation between coronal compactness (i.e., spectral hardness) and the covering fraction of cold, reflecting material. The correlation between ‘reflection fraction’ and soft X-ray flux, however, appears to be more universal. Furthermore, low flux, hard state observations—taken over a decline into quiescence—show that the Fe line, independent of ‘reflection fraction’, remains broad and at a roughly constant equivalent width, counter to expectations from Advection Dominated Accretion Flow models. All power spectral densities (PSD) of the hard state X-ray lightcurves are describable as the sum of just a few broad, quasi-periodic features with frequencies that roughly scale as coronal compactness, ℓ_c , to the $-3/2$ power. This is interpretable in a simple, toy model of an *efficient* spherical corona as variations of $\ell_c \propto R_t$, where R_t is the ‘transition radius’ between the corona and an outer thin disc. Similar to observations of Cyg X-1, time lags between soft and hard variability anti-correlate with coronal compactness, and peak shortly after the transition from the soft to hard state. A stronger correlation is seen between the time lags and the ‘reflection fraction’. These latter facts might suggest that the time lags are associated with the known, spatially very extended, synchrotron emitting outflow.

1 INTRODUCTION

1.1 Coronal Models

Most galactic black hole candidates (BHCs) show transitions between spectrally soft states and spectrally hard states. Hard spectral states appear to occur at bolometric luminosities $\lesssim 5\%$ of the Eddington limit, L_{Edd} , while soft spectral states occur at higher luminosities (Nowak 1995). A possible interpretation of this luminosity sequence is that state transitions are related to changes in the mass flow, \dot{M} , through the accretion disc. The nature of the transition between states, and, equally importantly, the geometry of the accretion flow within any given state, is still uncertain and a matter of vigorous debate (see Done 2001 for a review).

Most current models favor Comptonization as the major physical process to produce the observed hard state X-ray spectrum (although see Markoff et al. 2001). In these models, soft photons from an accretion disc are Compton-upscattered in a hot ($kT_e \sim 150$ keV), thermal electron plasma, the accretion disc corona (ADC). Early models of this type usually assumed that the ADC sandwiched a clas-

sical Shakura & Sunyaev (1973) accretion disc (Sunyaev & Trümper 1979; Haardt & Maraschi 1993). It has generally been assumed that this corona is produced via magnetohydrodynamical instabilities (Balbus & Hawley 1991; Stone et al. 1996). It has been shown, however, that such a sandwich geometry does not reproduce the observed X-ray spectra. The temperatures required to produce the hard power law cannot be reached since reprocessing of $\sim 50\%$ of the hard Comptonized radiation results in a very large Compton cooling rate of the corona (Dove et al. 1997a).

In recent years, a large set of different ADC geometries have been proposed in order to circumvent the “heating problem”. All of these models have small covering factors for the ADC or attempt to otherwise reduce the fraction of reprocessed hard radiation returning to the ADC as soft radiation. Models discussed include: patchy, static, coronae above the accretion disc (Stern et al. 1995; Gierliński et al. 1997; Poutanen & Fabian 1999); in- or outflowing coronae where the amount of reprocessed radiation is decreased due to relativistic beaming (Shrader & Titarchuk 1999; Beloborodov 1999); heavily ionized reflector models (Nayakshin & Dove

Table 1. Observing log of the observations of GX 339–4.

Obs.	Date (y.m.d)	Exp. ^a (s)	3–9 keV ^b	9–20 keV ^b 10 ^{−9} erg cm ^{−2} s ^{−1}	20–200 keV ^c	Optical M _B , M _V , M _I	Radio mJy
P20181_01	1997.02.03	5000	1.06	1.02	4.95		$d9.1^{+0.2}_{-0.2}, 7.0^{+0.7}_{-0.7}$
P20181_02	1997.02.10	10500	0.94	0.91	4.58		$d8.2^{+0.2}_{-0.2}, 6.3^{+0.7}_{-0.7}$
P20181_03	1997.02.17	8200	0.90	0.87	4.53		$d8.7^{+0.2}_{-0.2}, 6.1^{+0.7}_{-0.7}$
P20056_01	1997.04.05	2200	0.91	0.87	4.29		
P20056_02	1997.04.10	2100	1.09	1.03	4.77		
P20056_03	1997.04.11	1800	1.09	1.02	4.77		
P20056_05	1997.04.15	1800	1.16	1.06	5.05		
P20056_06	1997.04.17	1300	1.19	1.11	5.18		
P20056_07	1997.04.19	2100	1.17	1.07	4.75		
P20056_08	1997.04.22	2000	1.10	1.06	4.42		
P20181_04	1997.05.29	9900	0.60	0.59	3.02		
P20181_05	1997.07.07	10000	0.24	0.25	1.48		
P20181_06	1997.08.23	11400	0.72	0.71	1.84		
P20181_07	1997.09.20	10500	0.95	0.90	4.49		
P20181_08	1997.10.28	10500	0.62	0.47	3.21		
P40108_01	1999.01.12	12300	0.63	0.14	0.20		$e < 0.2, < 0.2$
P40108_02	1999.01.22	13100	0.53	0.12	0.20		$e < 0.2, < 0.2$
P40108_03	1999.02.12	6800	0.47	0.42	1.84	$f 17.9, 17.2, 15.9$	$e 4.6^{+0.1}_{-0.1}, 6.4^{+0.1}_{-0.1}$
P40108_04	1999.03.03	16600	$g 0.47$	0.45	2.40	$g 17.6, 16.9, 15.6$	$e 5.7^{+0.1}_{-0.1}, 6.1^{+0.1}_{-0.1}$
P40108_05	1999.04.02	9200	$g 0.49$	0.48	2.75		$e 5.1^{+0.1}_{-0.1}, 4.8^{+0.1}_{-0.1}$
P40108_06	1999.04.22	13100	0.23	0.23	1.31		$e 3.1^{+0.0}_{-0.0}, 2.2^{+0.1}_{-0.1}$
P40108_07	1999.05.14	9800	0.08	0.07	0.38		$e 1.4^{+0.0}_{-0.0}, 1.3^{+0.1}_{-0.1}$

^aExposure times rounded to the closest 100 s; ^bPCA Flux; ^cHEXTE Flux, normalized to PCA; ^d8.6 GHz, 0.8 GHz data, from Wilms et al. (1999); ^e8.6 GHz, 4.8 GHz data, from Corbel et al. (2000); ^{f,g}data from YALO telescope, 5–6 days after X-ray observation (*f*) and within ± 1 day of X-ray observations (*g*), courtesy C. Bailyn and R. Jain; ^hGIS Flux 0.39 and 0.38×10^{-9} erg cm^{−2} s^{−1}, respectively

2001; Nayakshin & Kallman 2001; Done 2001); and models in which the ADC and the accretion disc are physically separated. In the latter models, the ADC is typically represented by a very hot, geometrically thick accretion disc in the central regions around the black hole, surrounded by a cold, geometrically thin and optically thick accretion disc. Models of this type are the “sphere+disc” models of Dove et al. (1997b)— where it is assumed that the matter flowing through the corona is efficiently converting its potential energy into radiation— and the Advection Dominated Accretion Flows (ADAFs; e.g., Esin et al. 1997)— where most of the potential energy of the accreting matter is advected into the black hole. These latter models also postulate that a large fraction of the seed photons for Comptonization come from synchrotron radiation, due to the motion of the hot electrons in the magnetic field of the advective flow.

A further complication of ADC models is the interface between the cold accretion disc and the ADC. In “slab-like” ADC models, the high ionization parameter at the ADC-disc interface leads to the formation of an ionized transition layer which can strongly affect the reflectivity of the accretion disc (Ross & Fabian 1993; Nayakshin & Dove 2001; Nayakshin & Kallman 2001; Done 2001). The “sphere+disc” models, notably, fail to reproduce the observed iron fluorescence features, possibly due to the fact that any overlap between the accretion disc and the ADC is usually not modelled (Dove et al. 1998, although see Zdziarski et al. 1998). Finally, due to the closeness of the ADC to the central black hole, relativistic smearing of spectral features needs to be accounted for (Done & Życki 1999), although many models have ignored such effects.

Observationally, the situation is equally challenging. For “sphere+disc” models, radiatively efficient spherical models have suggested coronal radii as small as $\sim 30 GM/c^2$ (Wilms et al. 1999), while ADAF models typically prefer radii $\gtrsim 200 GM/c^2$ (Esin et al. 1997). Attempts to measure the coronal size mostly have been unsuccessful (Nowak et al. 1999a; Nowak et al. 1999c). On the other hand, attempts to model the observed broad band X-ray and γ -ray spectra with the ADC models have generally been quite successful (Dove et al. 1998; Gierliński et al. 1997; Gierliński et al. 1999; Zdziarski et al. 1998; Shrader & Titarchuk 1999). Many fundamentally different Comptonization models appear to give equally good fits to the data, thus making a decision between these models from a purely observational point very difficult. One potential discriminant among models has emerged with the suggestion of Zdziarski, Lubinski, & Smith (1999) that there is an *anti-correlation* between the spectral hardness of hard state BHC spectra and the covering fraction of cold, reflecting material (the so-called ‘ Γ - $\Omega/2\pi$ correlation’, where Γ is the photon number flux power law spectral index, i.e., $F_\gamma \propto E^{-\Gamma}$, and $\Omega/2\pi$ is the covering fraction of the cold reflector). Different power-law+reflection models which fit the same data equally well, have implied very different underlying fit parameters. (Contrast the fits of GX 339–4 data presented by Wilms et al. 1999 to those presented by Revnivtsev, Gilfanov, & Churazov 2001.) Finally, we note that the “Comptonization paradigm” itself has recently been challenged, with Markoff et al. (2001) postulating that synchrotron radiation from the radio outflow/jet, now observed in many BHC systems during the hard state, might well contribute a large fraction of the observed X-ray flux.

1.2 Observations of GX 339–4

The galactic black hole GX 339–4 is well-suited to perform a new study of the relative merits of different accretion disc models, as it is the only persistent source that has been observed in all spectral states of BHCs (Ilovaisky et al. 1986; Grebenev et al. 1991; Miyamoto et al. 1991; Méndez & van der Klis 1997; Wilms et al. 1999). Furthermore, the emission from GX 339–4 is likely completely dominated by the accretion flow, all the way from radio through gamma-ray wavelengths, and it shows strong correlations among these energy bands (Hannikainen et al. 1998; Wilms et al. 1999; Corbel et al. 2000; Fender 2001). In general, radio emission at $\lesssim 10$ mJy levels is present, is positively correlated with the X-rays in the hard state, and is quenched during the soft state (Hannikainen et al. 1998; Fender et al. 1999; Corbel et al. 2000). Brightness temperature arguments suggest that, during the hard state, the radio emitting outflow must extend to $> 10^{12.5}$ cm (Wilms et al. 1999). For the hard state, the optical light from this system is likely dominated by the accretion flow onto the compact object as well, with a large fraction of the hard state optical flux possibly being synchrotron emission from the extended outflow (Imamura et al. 1990; Steiman-Cameron et al. 1990).

In this paper we apply a variety of spectral models and timing analyses to 22 observations of GX 339–4 obtained with the *Rossi X-ray Timing Explorer* (RXTE), some of which were also simultaneous with the *Advanced Satellite for Cosmology and Astrophysics* (ASCA), optical, and/or radio observations. The observation log, with fluxes in selected energy bands, is presented in Table 1. Assuming isotropic emission, a $4 M_{\odot}$ compact object mass, and a distance of 4 kpc, the 3–200 keV luminosities of the hard state observations listed in Table 1 correspond to 2×10^{-3} – $0.03 L_{\text{Edd}}$.

The observations were chosen for analysis as follows. Eight of these observations (P20181) were originally extensively analyzed by us (Wilms et al. 1999; Nowak et al. 1999b). We had found that those data, with the exception of the faintest observation, showed few differences among their variability properties (Nowak et al. 1999b), and that their spectra could be well-fit by either a sphere+disc coronal model, or by a power-law plus ionized reflection model (Wilms et al. 1999). For the latter spectral model, we did not find a hardness-reflection fraction anti-correlation, but instead we found a hardness-ionization parameter anti-correlation. This is in contrast to the results of Revnivtsev, Gilfanov, & Churazov (2001), who, *analyzing the same data* with a power law+reflection model (with gaussian smearing applied to mimic relativistic smearing), did find the suggested anti-correlation. We have chosen to reanalyze these observations, as well as seven others (P20056) that represented the brightest and softest hard state observations presented by Revnivtsev, Gilfanov, & Churazov (2001).

We present seven other observations (P40108) that are original to this work. All of these observations were performed simultaneously with radio observations (see Corbel et al. 2000), two were performed simultaneously with *Advanced Satellite for Astrophysics and Cosmology* (ASCA) observations, and three were performed near-simultaneously with optical monitoring. An additional five observations exist in this series (again, with a number of simultaneous radio,

optical, and ASCA observations); however, these latter observations, in contrast to the first seven, are too faint to perform useful timing analyses. These fainter observations will be discussed in a future work (Corbel et al. 2001; in preparation).

1.3 Outline

In §2 we discuss the spectral analysis in detail, concentrating on the results obtained with three different Comptonization models. Before discussing the analyses in detail, however, we begin with a comparison of the relative strengths and weaknesses of each of these models. In §3 we describe the timing behaviour of GX 339–4, and correlate this behaviour with the results of our spectral analyses. Twenty out of twenty two of our observations occurred in the hard state. In §4 we describe our analysis of the two soft state observations. We assess in §5.2 the robustness of our fits by presenting ratios of the GX 339–4 data to observations of the Crab nebula and pulsar. We explore the reality of the hardness-reflection fraction anti-correlation in §5.3. In §5.4, we present a new, simple coronal model that reproduces some of the coronal-temporal correlations that we find in §3. We discuss the implications of our results for ADAF models in §5.5, and we briefly discuss alternative models to thermal Comptonization in §5.6. We summarize our results in §6.

Our results rely on many observations with several satellites. In order not to deter the reader from the results of the analysis with the technicalities of the data extraction, we present our data extraction strategies separately in Appendix A.

2 SPECTRAL FITS

2.1 The Blind Touching the Elephant: The Relative Merits of Various Coronal Models

Here we discuss the Comptonization codes of Poutanen & Svensson (1996), Coppi (1999), and Dove, Wilms & Begelman (1997a). Although each has been used separately to fit various BHC spectra, this work is the first to attempt to systematically compare several of them. All three will be used in fits of the GX 339–4 data. Each model has unique attributes and considers one or more facets of the Comptonization problem more ‘correctly’ or ‘completely’ than the others; however, none are truly fully self-consistent models.

The code of Poutanen & Svensson (1996) (`compps` in the X-ray spectral fitting package, XSPEC; Arnaud 1996) is essentially a ‘one-zone’ model in that it considers injection of (either blackbody or multi-temperature disc blackbody; Mitsuda 1994) seed photons with a prescribed flux and a fixed geometry into a corona of uniform optical depth and temperature and/or uniform distribution of non-thermal electrons. The corona also has a fixed geometry, although a variety of geometries are considered. A fraction of the escaping photons can be reflected off of cold, partially ionized material; however, this fraction is not self-consistently determined, nor are any of the reflected photons further reprocessed by the corona. Smearing of the reflection due to relativistic disc motion and gravitational effects, however, can be applied. The Fe edge is modelled in the reflection, but the Fe line is

not. Furthermore, the temperature of the corona and its (photon-photon collision produced) electron-positron pair optical depth are not self-consistently calculated, and must be checked *a posteriori*.

The model of Coppi (1999), available from that author as the XSPEC model **eqpair**, does calculate a self-consistent coronal temperature and pair optical depth by using the coronal compactness (proportional to energy released in the corona divided by its radius) as the fundamental fit parameter. Furthermore, it allows one to specify both a thermal and non-thermal compactness for the corona, as well as a compactness for the (blackbody) seed photons. A spherical corona with seed photons distributed according to the diffusion equation is modelled; therefore, *all* the seed photons pass through the corona. Reflection is implemented in a similar manner to the **compps** model, but smearing of the reflection is not considered. We will use this model extensively in the following sections, and we will present coronal compactness, ℓ_c , instead of coronal temperature, kT_e , coronal y -parameter, or power-law photon index, Γ , as a fundamental fit parameter.

The coronal model of Dove, Wilms, & Begelman (1997a), available from those authors as the XSPEC model **kotelp**, utilizes Monte Carlo spectra calculations that are then stored in an interpolation grid. For a given seed photon spectrum and geometry and a given coronal geometry and initial optical depth, the non-uniform coronal temperature distribution, pair optical depth, energy balance between corona and disc, and reflection fraction— with subsequent re-Comptonizations/re-reflections of this component— are all self-consistently calculated. In this work we shall use the ‘sphere+disc’ geometry described by Dove et al. (1998), i.e. a multi-temperature disc blackbody seed photon distribution with $kT(R) \propto R^{-3/4}$ and maximum temperature of $kT = 150$ eV emanating from an outer thin disc surrounding a central spherical corona. (Other geometries and seed photon distributions are possible.) Again, the fundamental parameter is the coronal compactness, ℓ_c , relative to the disc compactness (fixed to 1), not the average coronal temperature. For $\ell_c \lesssim 1$, the *intrinsic* energy generation of the disc dominates the system flux. For $\ell_c \gtrsim 1$, the seed photon spectrum is dominated by hard X-rays reprocessed by the disc (Dove et al. 1997b). The Fe line and edge are both calculated as part of the reflection component; however, in current implementations no relativistic smearing and only solar abundances are considered.

As is evident from the above capsule summaries, the various models do represent to some extent the “blind man touching the elephant”, each feeling out a different portion of the puzzle. Even though the **compps** model represents a ‘one zone’ corona, it is still the most flexible in terms of geometry of both the corona and the properties of the reflector. (Given sufficient computer resources to run grids of models **kotelp** can be equally flexible.) The **compps** model, however, lacks the self-consistent energy balance provided by **eqpair** or **kotelp**. The **eqpair** model has self-consistent energy and pair balance, but lacks the flexible geometry of the other two models. The **kotelp** model self-consistently determines the coronal energy balance, the seed photon flux (i.e., intrinsic disc flux vs. reprocessed flux), and the reflected component, but is the least flexible of the models in terms of currently available fit parameters.

2.2 Considerations for Model Fitting

A complication in utilizing the above models is that degeneracies are common, especially as regards the issue of reflection. Models of the Fe line/edge region are strongly affected by assumptions concerning the Fe abundance, the shape of the seed photon and incident hard spectrum, the reflection fraction, the reflector’s ionization parameter, the coronal geometry and outflow properties (e.g., Beloborodov 1999), and the reflector inclination. All but the first of this list could easily vary from observation to observation. (The reflector inclination could vary due to disc warping effects; Pringle 1996, Maloney & Begelman 1997.) Indeed, we have found adequate fits *for the same observation* with reflection fractions ranging from 0 to 1, Fe line equivalent widths ranging from 50–400 eV, coronal temperatures ranging from 20–200 keV and coronal optical depths ranging from 0.1–3.

Another consideration perhaps unfamiliar to those who do not practice X-ray astronomy and perhaps too readily accepted by those who do, is that model fits often have reduced χ^2 substantially below unity. This is in part due to the adoption of systematic errors (see the Appendix), and indicates that we are fitting some systematic features of the satellite response matrices. Fits to the (presumed power-law) Crab nebula plus pulsar clearly indicate the presence of systematic errors in the *PCA* response. Furthermore, without systematic errors, the low energy *PCA* data would dominate the fits, while the high energy *HEXTE* data, useful for measuring coronal temperatures and optical depths, would add very little statistical weight.

Obtaining a reduced χ^2 substantially below one indicates that an *individual* observation is over-parameterized. In the fits described below, we try to minimize any over-parameterization by freezing numerous parameters, especially in the line region, and we have tended to adopt fairly small systematic errors in high signal-to-noise regions of the spectrum (e.g., below 4 keV). The reduced χ^2 for the fits we present are always > 0.6 (cf. Revnivtsev, Gilfanov, & Churazov 2001). We would consider this too small if we were fitting a single observation; however, we are concerned with the *relative* trends of the fit parameters. Here we consider 20 separate, but uniformly measured and uniformly fit hard state observations. For example, small differences in the line region, even when some fraction of this region represents systematic effects, can be very statistically significant given the large effective area of the *PCA*. *Differences* in fit parameters, therefore, can be meaningful. Even then we endeavor not to over-interpret the parameter trends (see, for example, the discussion of Fig. 5). To give the reader some indication of the role played by systematic errors, in Table A1 we present a set of fits for observation P20181_01 (italicized), where we adopt no systematic errors. The error bars for parameters associated with narrow features (e.g., line widths) decrease somewhat. Overall, however, the “bestfit” parameters are not substantially changed, although the χ^2 has greatly increased.

Given the above concerns about model degeneracies and systematic errors, we explicitly examine the ratios of our data to those from the Crab nebula and pulsar. We discuss the implications of these comparisons for the interpretation of our fits in §5.2. We further discuss the relative parameter trends in the sections below.

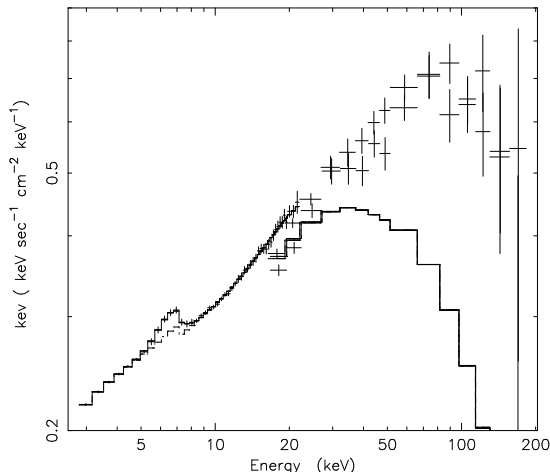


Figure 1. Unfolded energy spectrum of GX 339–4 (P40108_03) with the *eqpair* Comptonization model fitted to the *PCA* data only. The *HEXTE* data, assuming the model fit to the *PCA* data, is also shown assuming a relative normalization constant of 0.9 (see Appendix) for both the *HEXTE* A and B clusters as compared to the *PCA*. (Here error bars are $1\text{-}\sigma$.)

2.3 PCA Fits: *eqpair*+gauss

As discussed by Wilms et al. (1999), there typically has been a difference between the best-fit photon indices for *PCA* and *HEXTE* observations of the Crab pulsar and nebula of $\Delta\Gamma \gtrsim 0.1$. Recent *PCA* response matrices have slightly decreased this discrepancy; however, differences still remain. Partly for this reason, numerous authors have chosen not to include the *HEXTE* data in their fits of GBHC spectra (e.g., Revnivtsev, Gilfanov, & Churazov 2001). Here we briefly explore whether this is justified.

For our fits to *PCA* data, we have applied the *eqpair* Comptonization model with an additional gaussian line profile with a peak energy fixed at 6.4 keV. We further have fixed the blackbody seed photon compactness to be 1, the reflection to be from cold, neutral material with solar abundances, the angle of the reflecting medium with respect to our line of sight to be 45° , and the compactness of the non-thermal electrons to be 0. The fit parameters are therefore the compactness of the thermal electrons, the coronal optical depth, the seed photon blackbody temperature, the overall normalization, the line width, and the line amplitude. Folding in the systematic uncertainties described in the Appendix, these models yield extremely good fits to all the hard state observations, with typical reduced $\chi^2 \sim 0.3$. The fitted lines have widths of $\sigma \approx 1$ keV and equivalent widths ranging from 100–300 eV. The reflection fractions range from $\Omega/2\pi \approx 0.3\text{--}0.6$. The seed photon temperature is typically ≈ 600 eV, the coronal optical depth is typically ≈ 2 , and the coronal compactness is typically $\ell_c \approx 1\text{--}7$, which here implies coronal temperatures of tens of keV.

Fig. 1, which presents the unfolded spectrum for observation P40108_03, shows that these fits fail utterly to reproduce the *HEXTE* data, even accounting for likely systematic differences between *PCA* and *HEXTE*. The ‘unfolded spectrum’ shows the best fitting model, here plotted as $E^2 \times F_\gamma(E)$, multiplied by the ratio of the data in detector space to the spectral model folded through the experimental response function of the detectors. It is important to note in

Fig. 1 that the apparent visual significance of narrow spectral features should not be taken too strongly. An ‘unfolded spectrum’ has a tendency to exaggerate the *assumed* spectral features, especially those with widths comparable to or narrower than the instrumental resolution. In this instance, however, the unfolded spectrum does highlight the complete inadequacy of the extremely well-fitting *PCA* model in describing the broad-band *HEXTE* data.

2.4 PCA+HEXTE Fits: *kotelp* Models

We fit the simultaneous *PCA* and *HEXTE* data with the *kotelp* model with a ‘sphere+disc’ geometry as described by Dove et al. (1998). Here we choose to average the spectrum over inclination angles $\mu \equiv \cos \theta = 0.4\text{--}0.6$. These models do not adequately fit the data, and typically produce reduced $\chi^2 > 3$, primarily due to large, broad residuals in the Fe line/edge region, as one might expect for a relativistically broadened line. (We previously had noted this for *kotelp* fits to *RXTE* data of Cyg X-1; Dove et al. 1998.)

In order to mimic such a line for the *kotelp* model, we performed a series of fits where we added a narrow, fixed energy and negative amplitude gaussian function to remove the ≈ 30 eV equivalent width (EW) line produced by the code. We then added a broad gaussian function with peak energy fixed at 6.4 keV, and refit the models. Fitted parameters are presented in Table A1 in the Appendix. These models produced markedly improved fits, with reduced χ^2 ranging from 0.7–2.5, with an average reduced χ^2 of 1.6. The three faintest observations fit best. Most observations show negative residuals, as might be expected from an unmodelled edge, near 10 keV. A large fraction of χ^2 , however, comes from the 3–4 keV region, where 1999 observations show positive residuals, i.e., a soft excess, and 1997 observations show negative residuals.

We note that if we instead fit near edge-on *kotelp* models, the P20056 fits improve by $\Delta\chi^2 \approx 10$, since the contribution of the seed photon spectrum is reduced compared to the Comptonized spectrum, and hence the negative 3–4 keV residuals are reduced. The P20181 observations fit approximately the same, but the 1999 fits become much worse as the 3–4 keV excess increases. If we instead choose a nearly face-on *kotelp* model, as the seed photon spectrum is now emphasized compared to the Comptonized spectrum, the positive 3–4 keV residuals are then reduced. Such fits to the 1999 observations improve by $\Delta\chi^2 \approx 30$. The fits to the 1997 observations, however, become much worse. We discuss these points further in §2.5, §2.6, and §5.2.

Fitted compactnesses range from 1–7, and fitted optical depths range from 1–1.6. These parameters translate to average coronal temperatures of 90–170 keV. (Note, however, that face-on *kotelp* models produce lower compactnesses and higher optical depths, resulting in a corona with a lower temperature; see §2.6.) Equivalent widths of the added broad line range from 110–220 eV, and widths of the lines range from $\sigma \approx 0.4\text{--}0.9$.

Two trends stand out from these fits. As Fig. 2 shows, there is a strong anti-correlation between compactness and 3–9 keV *PCA* flux for the 1997 hard state observations. In 1999, GX 339–4 is seen to have returned from the soft state with an initially very soft spectrum that hardened as the source faded, before beginning to soften slightly at very low

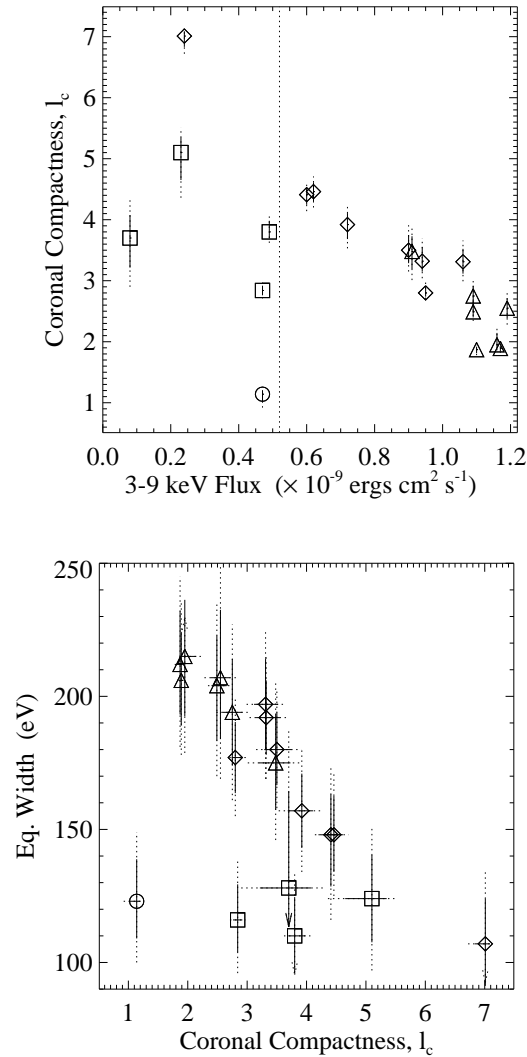


Figure 2. Results of the *kotelp* model fit to joint *PCA* and *HEXTE* data of GX 339–4. *Top:* Coronal compactness vs. *PCA* flux in the 3–9 keV band. *Bottom:* Equivalent width of the Fe line vs. coronal compactness. Throughout this work, unless otherwise noted, diamonds represent the 1997 hard state observations previously discussed by Wilms et al. (1999). Triangles represent 1997 hard state observations discussed by Revnivtsev, Gilfanov, & Churazov (2001). Squares represent 1999 hard state observations. Circles represent the first 1999 hard state observed after GX 339–4 returned from a protracted soft state. The dotted vertical line represents the lowest 3–9 keV *PCA* flux observed for the soft state observations discussed here. The dotted error bars are the 90% confidence limit (i.e., $\Delta\chi^2 = 2.71$ for one interesting parameter), and the solid error bars are equal to the 90% confidence level error bars divided by $\sqrt{2.71}$.

flux levels. As previously noted with *Ginga* data (Miyamoto et al. 1995), there is clear evidence for hysteretic behaviour. In 1997, GX 339–4 achieved a higher 3–9 keV flux, *without entering the soft state*, than the lowest 3–9 keV soft state flux measured shortly prior to the return to the hard state in 1999. The ‘overlap region’ between the hard and soft states appears to be in the 3–9 keV *PCA* flux range of $\approx 0.5\text{--}1.2 \times 10^{-9}$ ergs $\text{cm}^{-2} \text{s}^{-1}$. Of course, the issue of the ordering of the bolometric luminosities is less clear, especially since we have not measured the flux below 3 keV, which likely accounts for the largest fraction of the soft state flux. The observations represented by triangles in these figures are among the highest flux levels ever detected for the hard state of GX 339–4, whereas other ‘high state’ and ‘very

high state’ observations have exhibited substantially greater 3–9 keV fluxes (Belloni et al. 1999; Miyamoto et al. 1991).

The second correlation that stands out, also shown in Fig. 2, is the anti-correlation between the equivalent width of the broad line and the coronal compactness. In previous fits to a fraction of the 1997 hard state observations (diamonds; Wilms et al. 1999), utilizing *PCA* data only, such a correlation was *not* detected. Aside from not including *HEXTE* data, those previous fits utilized an earlier version of the *PCA* response matrix with larger systematic uncertainties. Here to some extent the Fe line equivalent width might be serving as a reasonable proxy for reflection fraction. If this is the case, however, then whereas a correlation is seen prior to the 1997 transition to the soft state, the correlation is apparently absent after the 1999 return to the hard state.

We considered two other combinations of models with the basic **kotelp** model in order to assess the robustness of the above correlations. Here we shall discuss only the highlights of the results. For both of these models, the line produced by the **kotelp** code was again subtracted as above. In the first case, we added the XSPEC **laor** model (Laor 1991), which gives the line profile for a relativistically broadened line from a disc rotating about a Kerr black hole^{*}. These models improved the reduced χ^2 of the fits to 0.7–2.1, with an average reduced χ^2 of 1.2. (The observation immediately following the return to the hard state, P40108_03, produced the worst fit, again due to a soft excess at $\lesssim 4$ keV.) The line energy, which was allowed to be a free parameter, ranged from 6.5–6.8 keV, and the line equivalent widths ranged from 150–350 eV. There essentially was no change from any of the trends and correlations discussed above.

For the second model, in addition to using the **laor** model to describe the line region, we also added an ionization edge at ≈ 8 keV. This further improved the fits to a reduced χ^2 ranging from 0.7–1.4, with an average of 0.9. (As before, observation P40108_03 was the most poorly fit due to a soft excess at energies $\lesssim 4$ keV.) The line energies were as above and their equivalent widths ranged from 100–270 eV. The additional ionization edge had an energy that ranged from 8.0–9.5 keV and that also was positively correlated with the **laor** line energy. The edge optical depth ranged from $\tau = 0.02$ –0.07. Although the line equivalent width correlations discussed above were slightly weakened, the trends shown in Fig. 2 again remain basically unaltered. Taking the above results as a potential signature of reflection changes, we turned to fits with the **eqpair** model.

2.5 PCA+HEXTE Fits: eqpair Models

For the joint fits to the *PCA* and *HEXTE* data discussed here, we used the exact same **eqpair** model as in §2.3, except that we instead fixed the Fe abundance to be 4 times solar, which is more consistent with the large line equivalent widths but low reflection fractions. (Lower or higher abundances, however, produced only slightly worse fits.) We found acceptable fits to the joint data with parameters very similar to the *PCA* only fits (§2.3); however, a completely different set of parameters described the joint data slightly better. These models, with a reduced $\chi^2 \approx 0.6$ –1.0, had seed photon temperatures in the range of 30–100 eV, coronal compactnesses in the range of 5–14 (yielding coronal temperatures of ~ 200 keV, given the typically fitted optical depth of 0.1–1), and reflection fractions of 0.1–0.5. Line widths were broad, and line equivalent widths were ≈ 80 –240 eV. Since these are considered to be the more “usual parameters” (see Poutanen, Krolik, & Ryde 1997), we present these results in Figs. 3–5 and give the parameters in Table A1.

As shown in Fig. 3, the same basic pattern of compactness vs. 3–9 keV flux was seen, i.e., higher fluxes yielded softer spectra, and GX 339–4 returned in 1999 from the soft

state with an initially soft spectrum. The variation, however, is less pronounced, especially on the return from the soft state in 1999. This is because for the **eqpair** model the seed photon temperature is not a fixed quantity. The relatively soft spectra for the first three 1999 hard state observations (P40108_03–05) are modelled with a combination of both low compactness and low seed photon temperature (≈ 30 eV). We note also that these three spectra indicate coronae that are pair-dominated, as the fitted initial electron optical depth was $\tau_{\text{es}} = 0.01$ (we set this value as a lower limit to the fits), but the total optical depths were $\tau \approx 0.3$. The error bars on the initial electron optical depths, however, were large, and non-pair-dominated plasmas are allowed. The soft positive residuals seen for observation P40108_03 with the **kotelp** model fits were absent with the **eqpair** fit.

Reflection fraction and Fe line correlations are readily noticed in Figs. 3 and 4. The most striking pattern is the reflection fraction, $\Omega/2\pi$, vs. the 3–9 keV *PCA* flux. There is a positive correlation of fitted reflection fraction with flux, except in the overlap/hysteretic region between the hard and soft states. There the reflection fraction is quasi-independent of flux, except at the very highest flux levels (triangles). Correlating the reflection fraction with compactness is less clear. Ignoring the P20056 observations (triangles), and the 3 lowest flux observations (P20181_05, P40108_06–07), no correlation would be seen between reflection fraction and compactness, as discussed by Wilms et al. (1999). Only by including the highest flux (triangles) and lowest flux observations does a possible anti-correlation between compactness and reflection fraction appear. Furthermore, the faintest three observations, taken by themselves, indicate exactly the opposite trend.

The Fe line equivalent width, as for the reflection fraction, is anti-correlated with compactness if one considers all the observations, but does not show this anti-correlation if one ignores the brightest (triangles) and faintest (P20181_05) observation (see Wilms et al. 1999). This is also seen by correlating the Fe line equivalent width with the reflection fraction. Prior to the 1997 transition to the soft state, reflection fraction and Fe line equivalent width are correlated, after the 1999 return to the hard state, there is a lower limit to the Fe line equivalent width of ≈ 150 eV. This is comparable to what we found for the **kotelp** fits discussed in §2.4, except that there the 1999 post-transition equivalent widths were consistent with the lowest equivalent width measured prior to the 1997 soft state transition.

There also is an apparent anti-correlation between physical line width, σ , and coronal compactness, as shown in Fig. 5. This is similar to the anti-correlation between spectral hardness and ‘smearing width’ claimed by Revnivtsev, Gilfanov, & Churazov (2001). The low reduced χ^2 of our fits, however, indicate that we may already be over-parameterizing the data. Furthermore, this anti-correlation is greatly weakened if we fit the brightest observations (triangles) with fixed line energies of 6.7 keV instead. The line widths then decrease by $\Delta\sigma \approx 0.2$ keV.

2.6 ASCA Observations

Two of the *RXTE* observations discussed in this work, P40108_04 and P40108_05, were obtained simultaneously

^{*} To some extent, the broad red tail of the **laor** line can offset differences between the *HEXTE* and systematically softer *PCA* detectors. A hard power law extrapolated backward from the *HEXTE* energy band to the *PCA* energy band could leave a soft excess, even if in reality no such excess existed.

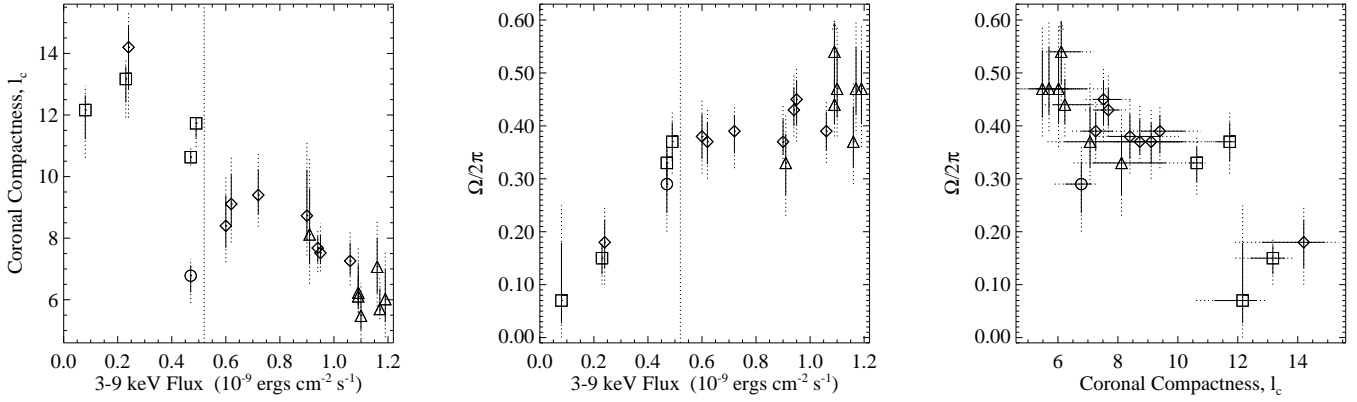


Figure 3. Results of the *eqpair* model fit to joint *PCA* and *HEXTE* data of GX 339–4. *Left:* Coronal compactness vs. *PCA* flux in the 3–9 keV band. *Middle:* Reflection fraction vs. *PCA* flux in the 3–9 keV band. *Right:* Reflection fraction vs. coronal compactness.

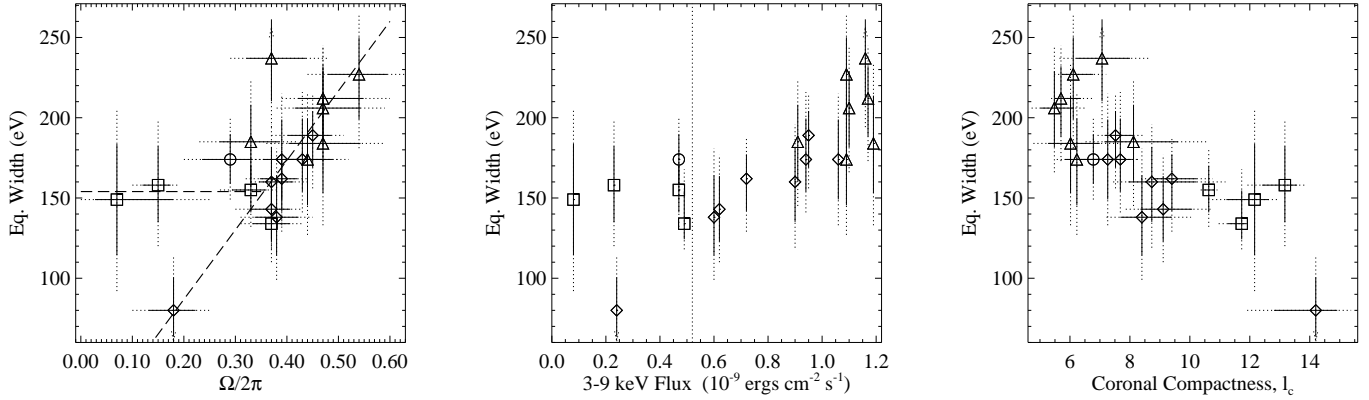


Figure 4. Results of the *eqpair* model fit to joint *PCA* and *HEXTE* data of GX 339–4. *Left:* Equivalent width of the Fe line vs. reflection fraction, $\Omega/2\pi$. Dashed lines show: the expected trend if the line equivalent width is proportional to reflection fraction (with 0 intercept), and the mean line equivalent width for the P40108 observations. *Middle:* Equivalent width of the Fe line vs. *PCA* flux in the 3–9 keV band. *Right:* Equivalent width of the Fe line vs. coronal compactness.

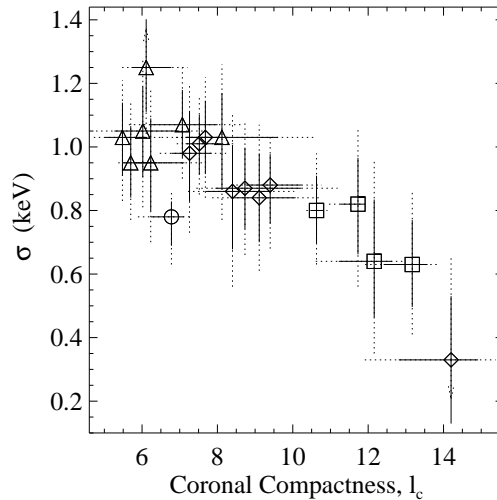


Figure 5. Width of the Fe line vs. the coronal compactness, for the *eqpair* model fit to joint *PCA* and *HEXTE* data of GX 339–4.

with *ASCA*. Compared to *RXTE*, *ASCA* had a narrower band pass (effectively 1–10 keV for observations obtained as late as 1999), an approximately 4 times smaller effective area, but a much higher spectral resolution ($\lesssim 0.2$ keV for these observations) and a lower background due to the nature of its instruments and its arcminute spatial resolution. Furthermore, as it is an independently calibrated instrument (see the mission web pages at <http://heasarc.gsfc.nasa.gov/docs/asca/ascagof.html> for a discussion of *ASCA* calibration issues), it provides a useful check of the *RXTE* results.

Analyzed independently of *RXTE*, these two *ASCA* observations can be fitted with models very similar to those employed by Wilms et al. (1999) to study three archival *ASCA* observations of GX 339–4. Specifically, these observations are well fit by a multi-temperature disc blackbody spectrum with peak temperature of ≈ 0.15 keV, a broken power law with a photon index ~ 1.8 below 4 keV and ~ 1.6 above, and a gaussian line at 6.4 keV[†]. These observations prefer Fe lines with equivalent widths of ≈ 220 eV and that are broad ($\sigma \approx 0.8$ keV), although the exact parameter values for the line do depend upon the fitted continuum model.

One might hope that including the *RXTE* data would remove enough of the ambiguities in the continuum model so as to further constrain the line model. In Fig. 6 we plot the residuals (detector space data divided by the model folded through the response matrices of the detectors) for an absorbed power law (N_H fixed to $6 \times 10^{21} \text{ cm}^{-2}$) fit to 1–22 keV data (1–10 keV in *GIS*, 2–10 keV in *SIS*, and 3–22 keV in *PCA*). Although both *ASCA* and *PCA* agree on the presence of a strong, broad line-like feature near 6.4 keV, there are clear systematic differences among the *GIS*, *SIS*, *PCA*, and *HEXTE* detectors. As we note in the Appendix, *PCA* and *HEXTE* yield different power law indices for observations of the Crab nebula and pulsar, with *HEXTE* giving a systematically harder index. The *ASCA* detectors were calibrated to yield Crab indices comparably hard to that found by *HEXTE*. Furthermore, both the *SIS* and *GIS* detectors show a break near 4 keV that is absent in the *PCA* data, as well as additional spectral structure near 1 and 2 keV.

Ignoring the *PCA* data, data from the *GIS*, *SIS*, and *HEXTE* detectors can be reasonably well-fit with the same disc blackbody, broken power law, plus gaussian line models mentioned above, but with an additional caveat. The power law above 4 keV (*uniform* from *ASCA* through *HEXTE* energy bands) is exponentially cutoff in the *HEXTE* bands at energies only $\gtrsim 80$ keV (i.e., the *highecut* model in XSPEC; see also Wilms et al. 1999). The reduced χ^2 for such models are ≈ 1.3 , with the greatest deviations coming from the 8–10 keV and 17–25 keV regions, where the model over-predicts the flux. An even better fit to just the *ASCA+HEXTE* data, however, can be obtained with a near face-on *kotelp* model

with the addition of a dust scattering halo, as is known to exist in this system from the work of Predehl et al. (1991), and references therein. We use the *dust* model from XSPEC, except here we *add* a component by fitting in XSPEC: absorption \times (model + [model – dust \times model]). This accounts for scattering of X-rays *into* our line of sight. The extra halo component has two parameters: f_{halo} , which is essentially the amplitude of the scattered component, and S_{halo} , which is related to size of the halo and effectively determines the energy ranges scattered by the halo. Residuals for these fits (allowing the N_H column to be a free parameter) are presented in Fig. 7, and the parameters are listed in Table A2.

These fits to the *ASCA+HEXTE* data are extremely good, with reduced $\chi^2 \approx 1$ for P40108_04. (The reduced χ^2 for P40108_05 is larger predominantly due to some disagreement between the *SIS* and *GIS* detectors in the 8–10 keV range.) The fitted N_H column (chosen to be the same for both the point source and dust spectrum) is in good agreement with prior measurements as well as considerations from optical extinction and 21 cm measurements (see the discussion and references of Zdziarski et al. 1998). The fractional contribution of the dust halo is $\approx 10\%$ at 1 keV, in agreement with the results of Predehl et al. (1991). The break in the *ASCA* spectra near 4 keV arises from a combination of the red tail of the Fe line, the curvature of the Comptonized spectrum towards low energy, the prominent blue tail of the seed photons due to the face-on disc, and the dust halo. We note that these face-on *kotelp* models, as compared to the models of §2.4, have slightly increased coronal compactnesses, but greatly increased coronal optical depths. This yields average coronal temperatures of ≈ 50 keV, as opposed to the ≈ 150 keV for the models of §2.4.

If we add the *PCA* data to the fits, the neutral hydrogen column and dust parameters do not greatly change, but the coronal compactness increases and the optical depth drops. The overall fit in terms of reduced χ^2 is not as good as for the *ASCA+HEXTE* fits alone, as is clear from Fig. 7. The detectors, as for Fig. 6, again show clear systematic differences. However, the level of residuals shown in Fig. 7, i.e., $\lesssim 1$ –5% for the *GIS*, *SIS*, and *PCA* detectors, are as low one can reasonably expect to achieve given the differing systematic uncertainties of these detectors.

3 TIMING ANALYSIS

As discussed in §1.2, these observations were selected partly because with them we were able to perform timing as well as spectral analyses. Timing analyses of the P20181 observations previously have been presented by Nowak, Wilms, & Dove (1999b) and Nowak (2000). Fourier power spectral densities (PSD) only of the P20181 and P20056 observations previously have been presented by Revnivtsev, Gilfanov, & Churazov (2001). The PSD fits presented below most closely follow the discussion by Nowak (2000).

Following the work of Wijnands & van der Klis (1999) and Psaltis, Belloni, & van der Klis (1999), Nowak (2000) suggested that the best representation of the hard state PSD of GBHC in general, and GX 339–4 in specific, was the sum of only a few, broad, quasi-periodic features. Nowak (2000) showed that a composite PSD of the seven brightest P20181 observations (which exhibit relatively uniform

[†] Note that, consistent with the analysis of *ASCA* observations of Cyg X-1 presented by Ebisawa et al. (1997), Wilms et al. (1999) searched for fits with *narrow* ($\sigma \sim 0.1$ keV) Fe lines. The fitted lines had equivalent widths ≈ 40 eV, and the fits yielded reduced $\chi^2 \approx 1$ for the faintest observations, but 1.4 for the brightest. As compared to the *ASCA* observations discussed here, the observations discussed by Wilms et al. (1999) had 3–9 keV fluxes that were approximately 0.3, 0.5, and 1.8 times as great.

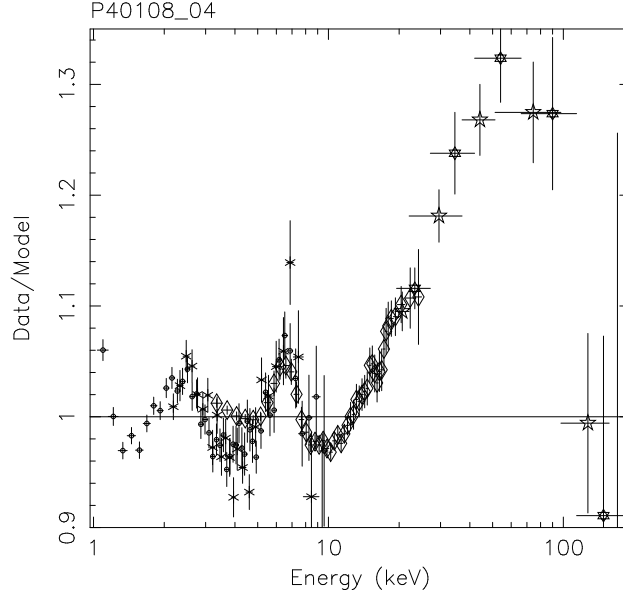


Figure 6. Residuals for an absorbed power law model fit simultaneously to the *SIS*, *GIS*, and *PCA* data (P40108_04). Circles and crosses are the *GIS* and *SIS* data, respectively. Diamonds are the *PCA* data. Stars are the *HEXTE* data (not included in the fit), with normalization constants chosen to match the *PCA* residuals. (Error bars here are $1\text{-}\sigma$ errors.)

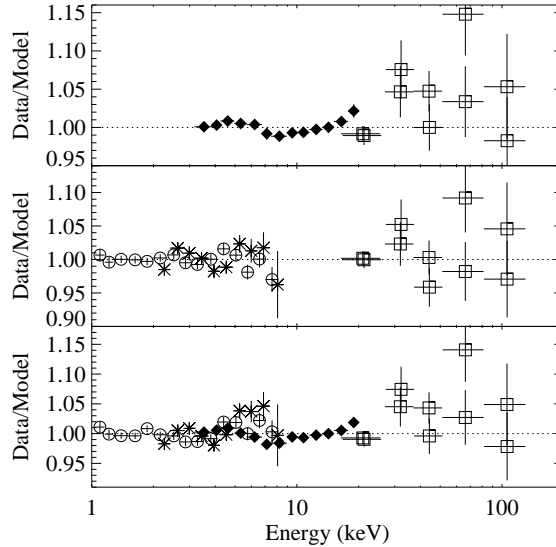


Figure 7. Residuals for corona plus dust scattering halo models (see text) fit to: *PCA* and *HEXTE* data (top); *GIS*, *SIS*, and *HEXTE* data (middle); and *GIS*, *SIS*, *PCA*, and *HEXTE* data (bottom). (Error bars here are $1\text{-}\sigma$ errors.)

variability properties; see Nowak, Wilms, & Dove 1999, and the discussion below), could be described by a zero frequency centered Lorentzian function with a cutoff frequency at 0.1 Hz, plus additional quasi-periodic oscillations (QPO) at frequencies 0.34 Hz (and its harmonic), 2.5 Hz, and 18 Hz. Following the suggestion of Psaltis, Belloni, & van der Klis (1999), the latter three frequencies might be the analogues of the ‘horizontal branch’, ‘lower kiloHertz’, and ‘upper kiloHertz’ QPO features seen in neutron star Z-sources. (For a description of the Z-source features, see van der Klis 1996.)

Here we considered each observation individually; therefore, we were unable to fit any features with peak frequencies

$\gtrsim 10$ Hz. Furthermore, we chose to fit a zero frequency centered Lorentzian function,

$$P(f) = \frac{A}{1 + (f/f_c)^2} \quad (1)$$

to the lowest ($\lesssim 0.1$ Hz) and highest ($\gtrsim 1$ Hz) frequency features. For the middle frequencies ($f \approx 0.3$ Hz), we fit a QPO function of the form

$$P(f) = \pi^{-1} \frac{R^2 Q f_0}{f_0^2 + Q^2 (f - f_0)^2} \quad (2)$$

where f_0 is the resonant frequency and Q is the quality factor, with $Q \approx \Delta f / f_0$ being the fractional width of the QPO. (For $Q \ll 1$, the maximum of $P(f)$ occurs at $f \gg$

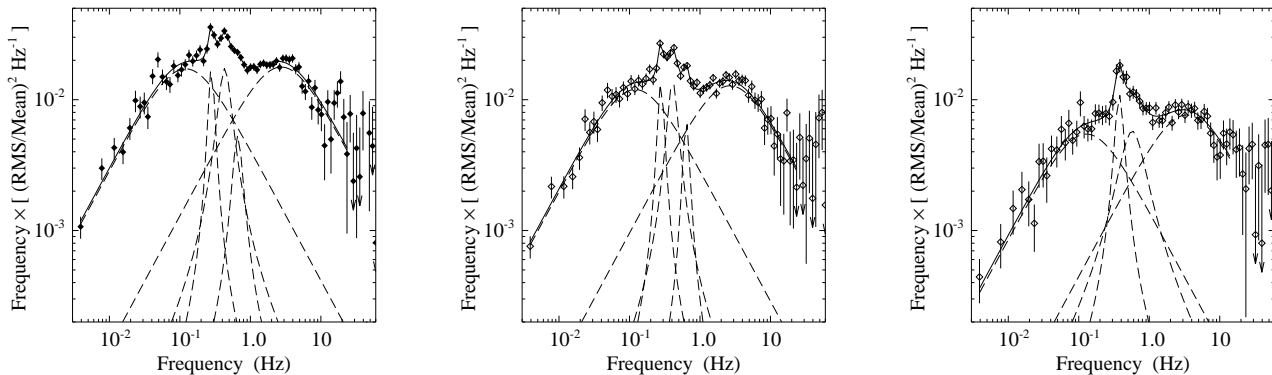


Figure 8. Fits to several PSD of GX 339–4. Solid line shows the best-fit model, while the dashed lines show the individual components of the model. *Left:* Observation P40108_05 in the 0–5 keV band. *Middle:* Observation P40108_05 in the 10–20 keV band. *Right:* Observation P20056_05 in the 10–20 keV band. (Error bars here are $1\text{-}\sigma$ errors.)

f_0 . Partly for this reason, we instead chose to fit a zero frequency centered Lorentzian function at high frequencies, where the signal-to-noise was low. A number of observations, most notably P20056_05, were better fit, however, with a high frequency QPO feature. We fit multiple QPO features in the 0.3 Hz range, so long as the χ^2 of the fits improved by more than 15 for each additional feature. Most PSDs required two such features, although several required three (Fig. 8).

Observation P40108_03 required only two features: the zero frequency centered Lorentzian function and a second feature which we identified as a QPO. As for all the other PSDs (with the exception of P40108_07; see below), this ‘QPO’ represented a distinct maximum in the plot of frequency times the PSD power (e.g., Fig. 8). P40108_07 also showed only two features, but they both were broad, they were widely separated in frequency, and they were of comparable amplitude in plots of frequency times PSD power. We therefore identified both of these features with the zero frequency centered Lorentzian functions.

Fig. 8 shows several examples of the PSD fits, and parameters for the high energy band fits are presented in Tables A4 and A5. In general, the root mean square (rms) variability was on the order of 30%, with the soft energy band showing slightly higher rms variability than the high energy band. Decreased variability at high energy has been argued by Revnivtsev, Gilfanov, & Churazov (2001), via “frequency resolved spectroscopy”, as indicative of the “reflection spectrum” having little variability. However, the PSD retains no phase information (which, in reality, could be a complicated mixture of components; see Nowak 2000). If a highly variable “power law” is 180° out of phase with a highly variable “reflection component” (as suggested for the “ $T\text{-}\Omega/2\pi$ ” correlation; Zdziarski, Lubiński, & Smith 1999), low variability would result at high energy.

There is some trend for the PSD fit components to show lower rms variability with higher frequency. This trend is most pronounced for the highest frequency fit component, as we show in Fig. 9. We also show in Fig. 9 the fitted frequencies plotted against the measured 3–9 keV flux. Whereas there is a large degree of variation among the low flux frequencies, there is relatively less frequency variation in the

‘hysteretic region’ above the lowest measured soft state 3–9 keV flux. The P20056 observations at very high flux show a slight upward trend in frequency. Observations P20181_05, P40108_06, and P40108_07, all at fairly low fluxes, all exhibit frequencies markedly lower than those exhibited by observations in the ‘hysteretic region’. Observation P40108_03, the first observation after the return to the hard state in 1999, although exhibiting a relatively lower variability amplitude, shows a sharp spike upward in characteristic PSD frequencies.

Note that although there are clear systematic trends, there is not a very large variation in the characteristic frequency of a given PSD feature. For example, the cutoff frequencies of the Lorentzian functions fit at high frequencies vary by less than a factor of 3 overall. di Matteo & Psaltis (1999) have argued that the limited range of frequency variations exhibited by GBHC argue for a comparably small (less than a factor of 2) variation in the (cylindrical) radial size scale of any central corona or in the size scale of any “transition radius” between an advection and non-advection dominated flow. Assuming that the highest observed frequency is generated in the outer, non-advection dominated disc (e.g., Psaltis & Norman 2000), 1.8 Hz implies a transition radius $\lesssim 270 GM/c^2$, for a $4 M_\odot$ central object. However, a feature with a frequency as high as 20 Hz, such as discussed by Nowak (2000) (which would not be detectable within these individual observations) would imply a radius $\lesssim 60 GM/c^2$. The rise of the characteristic PSD frequencies with increasing flux, followed by a plateau at high fluxes, is very reminiscent of the behaviour seen in the neutron star source 4U 1820–30 (Zhang et al. 1998; Kaaret et al. 1999). Such a plateau has been argued as evidence for the accretion disc extending inward all the way to its marginally stable orbit (Zhang et al. 1998; Kaaret et al. 1999).

In Fig. 9 we also show these frequencies plotted vs. the coronal compactness from the *kotelp+gauss* fits of Table A1. There is a clear trend for harder spectra to show systematically lower frequencies for all of the characteristic PSD features. Such a trend was noted by di Matteo & Psaltis (1999) and Revnivtsev, Gilfanov, & Churazov (2001), although those authors parameterized hardness by the photon index, Γ , and they did not include *HEXTE* data in their

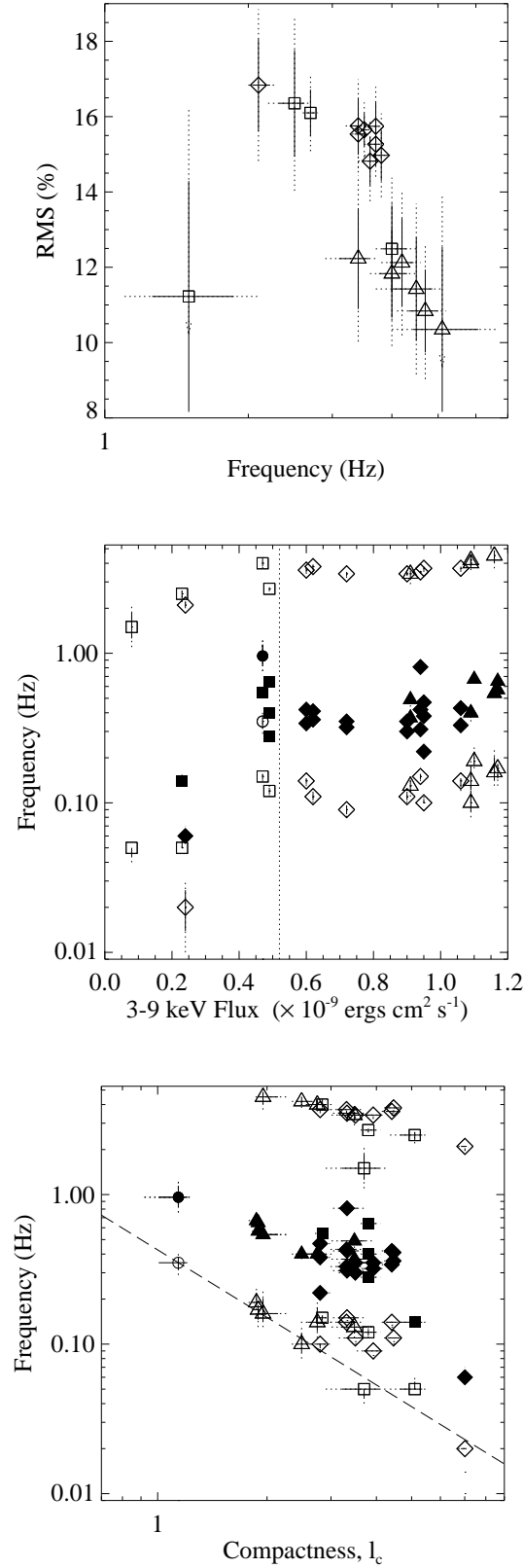


Figure 9. *Top:* rms variability vs. frequency for the highest frequency fit component to the PSD (10–20 keV band). *Middle:* Characteristic PSD frequencies (10–20 keV band) vs. PCA flux measured from 3–9 keV. Clear symbols are the roll-over frequency for the zero frequency centered Lorentzian functions (zfc-Lor₁ and zfc-Lor₂) in Tables A4 and A5. Solid symbols are the peak frequencies of QPO₁–QPO₃ in these tables. *Bottom:* Same frequencies as above, except here plotted vs. compactness from the `kotelp+gauss` fits of Table A1. Dashed line shows $f \propto \ell_c^{-3/2}$.

fits. Observations in the ‘hysteretic region’, which have relatively similar frequencies, deviate from this trend slightly. The overall behaviour, however, is roughly consistent with the PSD frequencies being proportional to $\ell_c^{-3/2}$ (although the highest frequency exhibits a slightly flatter trend). We comment upon this further in §5.4 below.

We have also calculated the average time lag between the variability in the 0–5 keV and the 10–20 keV energy bands. In general, the broad band variability of GBHC in their hard state shows the hard variability lagging behind the soft variability, with the lag increasing both for lower Fourier frequencies and for larger energy separations (Miyamoto & Kitamoto 1989; Miyamoto et al. 1992; Nowak et al. 1999; Nowak, Wilms, & Dove 1999; and references therein). As seen in Figs. 10, 11, and 12, the variability time lags span a large dynamic range from $\approx 10^{-3}$ sec at high Fourier frequencies, to ≈ 0.1 sec at low frequency. Various models have attributed this broad range of observed time delays to photon diffusion in a very extended corona (Kazanas et al. 1997), wave propagation in a disc (Nowak et al. 1999c), or temporally correlated flares covering an accretion disc (Poutanen & Fabian 1999). In order to both increase the signal to noise and to describe the overall characteristic behaviour of the time delays, we have averaged the calculated time lags over a range of a factor of 5 in Fourier frequency. The resulting average time lags are plotted vs. 3–9 keV flux in Fig. 10.

At the highest frequency, we see that the time delays are roughly consistent with being at a common minimum value of $\approx 10^{-3}$ Hz. We have previously argued that such a minimum value of the time delay sets a lower limit of roughly $30 GM/c^2$ for the size scale of any corona (Nowak et al. 1999c). For lower Fourier frequencies, we see that in the ‘hysteretic region’ time lags are relatively uniform from observation to observation. For observation P40108_03, coincident with the 1999 soft to hard state transition, there is an increase in the characteristic time lag. A very similar, but more dramatic, time lag increase also has been seen in the soft/hard state transitions (or ‘failed’ state transitions) of Cyg X-1 (Pottschmidt et al. 2000). At lower fluxes, the time lag is seen to drop.

Nowak, Wilms, & Dove (1999b) have previously argued that the simultaneous decrease in the characteristic PSD frequencies and in the time lags seen for observation P20181_05 (i.e., the lowest flux diamond points in the figures) argues against the flare models of Poutanen & Fabian (1999), where one expects the PSD time scales (i.e., inverse frequencies) and the time lags to be correlated. The trend exhibited by observation P20181_05 for the PSD time scales and time lags to be *anti-correlated* is seen to continue towards lower flux. Interestingly, the lowest flux observation shows that the power spectra averaged about 0.1 Hz and 4 Hz exhibit a lag of the soft variability behind the hard variability. We note, however, that as discussed by Nowak (2000), the net overall time lags could in fact be made up of several independent processes—which we would be averaging over in these figures—some of which have soft variability lagging hard variability, and some of which have hard variability lagging soft variability.

In Fig. 11 we show the time lags plotted against the coronal compactness from the *kotelp+gauss* fits of Table A1. Again, the plateau of the observations in the hys-

teretic region are apparent. The overall trend is for less compact/softer spectra to show longer time lags than more compact/harder spectra, albeit the faintest two observations deviate from this trend. This deviation for the faintest two observations is similar to that seen for the anti-correlation between ‘reflection fraction’ and compactness (from the *eqpair* fits) seen in Fig. 3. Plotting time lag vs. reflection fraction from the *eqpair* fits, we see that there is indeed a correlation between the two, as shown in Fig. 12, where higher reflection is seen to imply longer time lags of the hard variability behind the soft variability. If the reflection fraction is indeed truly measuring the relative amount of cold material being illuminated by the corona, then perhaps these data are arguing for low compactness/soft spectra being associated with a larger coronal size, which would yield longer time lags due to increased propagation or diffusion path lengths while simultaneously illuminating a larger region of the cold disc. We comment upon this further in §5.4.

4 SOFT STATE OBSERVATIONS

The soft state observations discussed here, P40108_01 and P40108_02, occurred shortly prior to a return to the hard state. A discussion of brighter soft state observations of GX 339–4, taken in early 1998 after the initial transition from the hard to soft state, can be found in Belloni et al. (1999). Observations P40108_01 and P40108_02 are very characteristic of ‘classic’ BHC soft states (Nowak 1995, and references therein). Both observations exhibit rms variability $\lesssim 3\%$ between $\approx 10^{-2}$ –1 Hz, and are totally dominated by Poisson noise residuals at higher frequencies.

In terms of their spectra, both observations show a strong soft excess at energies $\lesssim 8$ keV, with a $\Gamma \approx 2$ power law at higher energies; see Fig. 13. Such observations are typically well-described by a multi-temperature disc blackbody with maximum temperature of ≈ 1 keV, plus an additional power law, typically with a photon index $\gtrsim 2$. For an example of similar soft state BHC spectra observed with *RXTE*, we refer to our recent work on LMC X-1 and LMC X-3 (Nowak et al. 2001; Wilms et al. 2001). For these three soft state BHC, a broad and strong Fe line seems to be required (~ 1 keV width, ≈ 200 –900 eV equivalent width). As discussed by Nowak et al. (2001), there is some worry that such a line could be an artifact due to the phenomenological fit components, namely a multi-temperature disc blackbody and a power law, crossing over one another at an energy ~ 6 keV. A broad line could be required to remove an artificially created “inflection point”.

As with our LMC X-1 and LMC X-3 spectra, to assess this possibility for the soft spectra of GX 339–4, we turn to the *compps* model, and choose the “slab geometry” (i.e., a planar disc and corona, with seed photon injection occurring at the disc-corona interface at the midplane). As this model self-consistently calculates the high energy tail from the seed photon distribution and the coronal parameters, there is less worry about creating an artificial Fe line. In addition to the coronal parameters, we also allow for reflection from an ionized slab, with a relativistically smeared reflection profile. (We choose the $\beta = 10$ option in the *compps* model, and fix the inner and outer disc edge to be $6 GM/c^2$ and $10^3 GM/c^2$, respectively. The disc Fe abundance is set to 4, and the disc

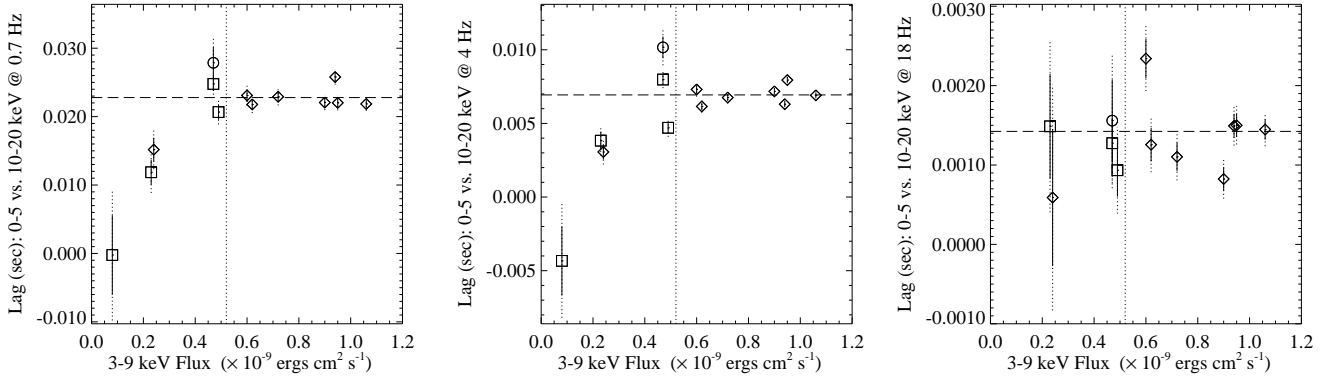


Figure 10. Time lags between variability in the 0–5 keV band and in the 10–20 keV band vs. PCA flux measured from 3–9 keV. Positive values indicate the hard band variability lagging behind the soft band variability. Dashed line corresponds to the mean time lag of all P20181 observations, excluding P20181_05. *Left:* Average frequency 0.7 Hz. *Middle:* Average frequency 3.7 Hz. *Right:* Average frequency 18 Hz.

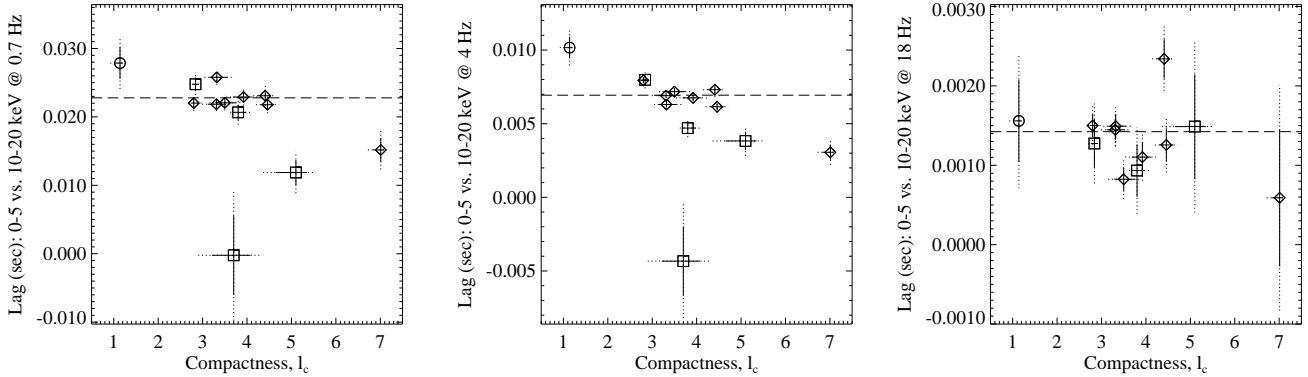


Figure 11. Same as in Fig. 10, except here plotted vs. compactness from the *kotelp+gauss* fits of Table A1. *Left:* Average frequency 0.7 Hz. *Middle:* Average frequency 3.7 Hz. *Right:* Average frequency 18 Hz.

inclination angle is frozen to 45° .) To model the line, we use the *laor* model in *XSPEC* (Laor 1991). Again, we set the inclination angle to 45° , and we freeze the inner and outer disc edge at their maximum values. We allow the line energy, normalization, and the disc emissivity index to be free parameters.

Results for these fits are presented in Table A3. The fits are very similar to our prior results for LMC X-1 and LMC X-3. Specifically, the disc inner edge temperatures are $kT_{\text{disc}} \approx 540$ eV, the fitted coroneae are very hot with $kT_e \approx 130$ keV, and they are also optically thin, with $\tau_{\text{es}} \approx 0.3$. In addition, the fitted Fe lines have energies ≈ 6.8 keV (consistent with ionized[†] iron), are very strong (600 to 900 eV equivalent widths[†]), and are very broad. Emissivity indices are > 5 , indicating lines that are *extremely* skewed towards the inner edge of the disc. The fitted reflection fractions,

[†] Note that we do not quote error bars for the line equivalent widths in Table A3, as the error bars are complicated functions of the other fit parameters, not just of the line normalization. Generally, the equivalent widths deviate from the best fit values by approximately -100 eV to $+500$ eV, depending upon what other parameters are allowed to vary.

in contrast to the line equivalent widths, are small, with $\Omega/2\pi \lesssim 0.2$. In this respect, these observations are similar to P40108_06 and P40108_07. The cold reflector, consistent with the line energies, is ionized.

The unfolded spectrum for observation P40108_01 is presented in Fig. 13. One question that arises, is the broad, large equivalent width line an artifact of our assumed model? For example, could the higher energy line with a sharp blue edge (due to the emissivity index being > 5), in reality be mimicking an unsmeared, neutral reflection edge at 7.1 keV? (The smeared, ionized edge is broader and extends to higher energies.) This would be expected if the reflection were due to a combination of an ionized, relativistic disc and cold, neutral matter much farther away from the compact object (i.e., a flared outer disc edge, the companion star, etc.). We have tried adding a neutral edge at 7.1 keV, and this does reduce the Fe line equivalent width, but only by ≈ 300 eV. As for our LMC X-1 and LMC X-3 observations (Nowak et al. 2001; Wilms et al. 2001), a fairly strong, broad line is a ubiquitous feature of all the models that we have attempted to fit to the GX 339–4 soft state data.

The other aspect that is to be noted about Fig. 13 is the possibility of a hardening at energies above ~ 80 keV. Due to

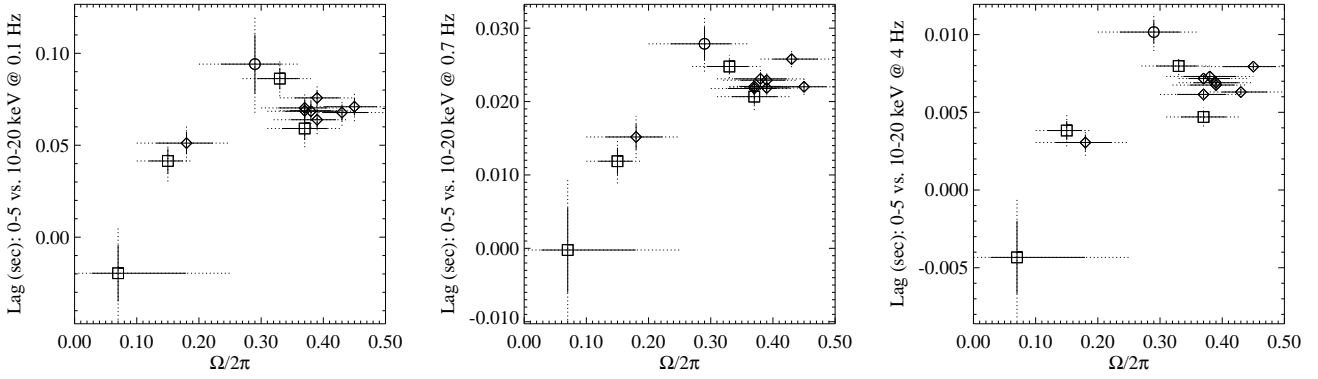


Figure 12. Same as in Fig. 10, except here plotted vs. reflection fraction from the `eqpair+gauss` fits of Table A1. *Left:* Average frequency 0.1 Hz. *Middle:* Average frequency 0.7 Hz. *Right:* Average frequency 3.7 Hz.

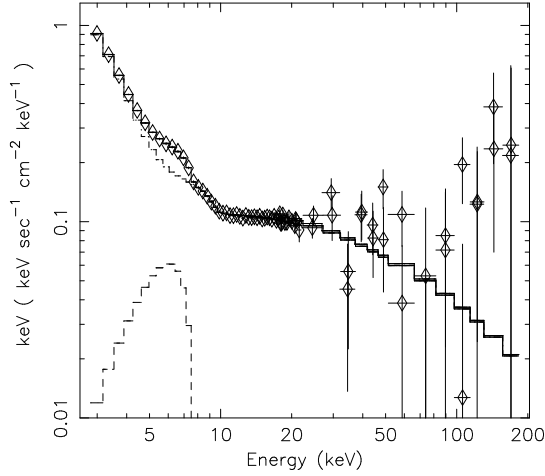


Figure 13. Unfolded energy spectrum of GX 339–4 (P40108-01) with the `compbs` Comptonization model fitted to the *PCA+HEXTE* data.

the very low hard flux, this hardening is entirely consistent with the uncertainties of the background measurement (see §5.6). We note also that we have used the `compbs` model to fit non-thermal Comptonization models, and obtain equally good, purely non-thermal fits. Thus, these data are unable to distinguish between a thermal and non-thermal electron distribution for the Comptonizing electrons.

5 DISCUSSION

5.1 Comparison to Previous Comptonization Models

As discussed in §1.1, the `compbs`, `eqpair`, and `kotelp` models endeavor to be physically motivated, realistic descriptions of Comptonization in compact object systems. The results that we have found here with these models are in many ways comparable to previous analyses of GX 339–4, as well as the spectrally similar source, Cyg X-1. For example, previous work with versions of the `compbs` model have found $\tau_{\text{es}} \sim 1$ and $kT \sim 100$ keV for Cyg X-1 (Poutanen et al. 1997b) and $\tau_{\text{es}} \sim 1$ and $kT \sim 50$ keV for GX 339–4 (Gierliński et al. 1997). Our own previous analysis of joint

PCA+HEXTE data of Cyg X-1 using the `kotelp` model found $\tau_{\text{es}} \sim 1$ and $kT \sim 90$ keV (Dove et al. 1998). On the other hand, we previously have found somewhat lower temperature ($kT \sim 20$ – 40 keV) and higher optical depth ($\tau_{\text{es}} \sim 3$) coronae for GX 339–4 (Wilms et al. 1999). However, unlike the aforementioned studies which were broad-band (≈ 2 – > 200 keV), the work of Wilms et al. (1999) fit the low energy (*PCA*) and high energy (*HEXTE*) data separately. Recent work fitting broad-band data of Cyg X-1 (Maccarone & Coppi, in prep.) with the `eqpair` model suggests similar coronal parameters as discussed above, and interestingly enough suggests at times a large equivalent width line (200 eV) with a low reflection fraction ($\Omega/2\pi \sim 0.2$), similar to what we have found for several of our observations of GX 339–4. Thus, there is at least general consensus that “realistic” Compton coronae models with $\tau_{\text{es}} \sim 1$, $kT \sim 100$ keV, and low reflection fractions, $\Omega/2\pi \lesssim 0.5$, provide reasonable descriptions of hard state black holes. (See §4 for references to recent work concerning soft state black holes, as well as Frontera et al. 2001, Gierliński et al. 1999.)

The above studies, however, for the most part considered either single observations, or a fairly small group of observations. Studies that have considered large groups of

observations analyzed in a systematic fashion (Wilms et al. 1999; Zdziarski et al. 1999; Revnivtsev et al. 2001) have tended to focus on more phenomenological models (e.g., power-laws with reflection). In addition, some of these studies have ignored or lacked high energy data above $\gtrsim 30$ keV (e.g., Revnivtsev, Gilfanov, & Churazov 2001, Zdziarski, Lubinski, & Smith 1999). Within these studies, there has been disagreement as to the interpretation of the results, even given the same data (see, for example, Wilms et al. 1999 and Revnivtsev, Gilfanov, & Churazov 2001). For this reason, as well as the concerns outlined in §2.2, in the following sections we examine our results more carefully. We begin by comparing our data to observations of the Crab nebula and pulsar.

5.2 Crab Ratios

In Fig. 14 we show the normalized ratio for observations P20056_07 and P20181_05 with respect to the Crab nebula and pulsar observation of 1997 September 05, and for observations P40108_03 and P40108_06 with respect to the Crab nebula plus pulsar observation of 1999 February 24. Compared to direct fitting of spectral models, such ratio plots have the advantage that they are relatively insensitive to the uncertainties in the calibration of the response matrix (Santangelo et al. 1998), although they are less sensitive to detailed features than spectral fitting (Kreykenbohm et al. 1999). The Crab ratios were generated by first subtracting the background from both the Crab and the GX 339–4 observations. The Crab spectrum was then multiplied by $E^{\Gamma_{\text{Crab}} - \Gamma_{339}}$ where $\Gamma_{\text{Crab}} = 2.18$ (see Appendix) and where $\Gamma_{339} = 1.73$ (i.e., the photon index for observation P20181_04). All spectra were then normalized to the same flux level at 10 keV. The Crab ratio was then obtained by dividing the GX 339–4 pulse height analyzer (pha) data by the modified Crab spectrum.

Fig. 14 shows most of the features that we have also found in the detailed spectral fitting and thus provides us with additional confidence that the general behaviour seen was not due to the response matrix uncertainty. Higher fluxes clearly yield softer spectra. Most of this variation is due to the soft X-rays, while the hard spectrum shape stays approximately constant. This is completely consistent with the results we previously obtained by modelling some of these data with a broken power-law model, where we found that the variation in the power-law index at softer X-rays was nearly twice as great than that at higher energies (specifically, see Table 5 of Wilms et al. 1999). We comment on this further in §5.3 below.

The Crab ratios also highlight the broad feature present at ≈ 6.4 keV, which in many models is consistent with a broad Fe line. In fact, fits with realistic Comptonization models always seem to require such a broad Fe line, as we first noted with fits to *RXTE* data of Cyg X-1 (Dove et al. 1998; who used a very early version of the *PCA* response matrix). With every subsequent revision of the *PCA* response matrix, realistic Comptonization models of both Cyg X-1 and GX 339–4 data have continued to require the presence of such a broad Fe line (Wilms et al. 1999). Taking the orthodox interpretation of the feature present in the Crab ratios as a broad Fe line, these ratios provide us with more confidence in some of the unusual results obtained in §2.5.

First, observation P20181_05 does indeed have the smallest equivalent width line, as was determined by the fits. In addition, the line is very narrow, and is essentially consistent with the *PCA* resolution. Also shown in Fig. 14 is the fact that the P40108 observations (i.e., the observations taken after the return to the hard state in 1999) indeed do have larger equivalent width, and for the most part broader, Fe lines. This is true even into quiescence, as shown by the Crab ratio for observation P40108_07. Note also that despite the fact that observation P40108_06 and P20181_05 have similar flux levels, similar fitted compactnesses, and similar fitted reflection fractions, the Crab ratio shows that P40108_06 has the clearly stronger and broader Fe line (cf. Revnivtsev, Gilfanov, & Churazov 2001). Again, however, as discussed in §2.5, the *fitted* physical line widths, σ , are complicated by one's assumptions for the line energy, the assumed reflection properties, and the continuum spectrum.

The Crab division is too insensitive to reveal some of the finer effects found by our modelling. For example, one trend seen in the *eqpair* fits to the data is for the temperature of the seed photons to decrease with decreasing flux. In the simple sphere+disc coronal model, one expects the approximate relationship $kT_{\text{bb}} \propto \ell_c^{-1/2} F_{\text{bol}}^{1/4}$, where F_{bol} is the total flux of the system (see §5.4 below). Thus, utilizing the results of Table 1 and A1, one expects an approximately factor of 2 change in the seed photon temperature from the brightest to the faintest observation, which is slightly larger than actually found for the P20181 and P20056 observations. Dramatic changes, however, are found for the first few observations after the return to the hard state in 1999, as we show in Fig. 15. The seed photon temperature is seen to be greatly lowered, and then slowly recovers to the previously observed trend over the course of the next several months of decline into quiescence. As discussed in §2, such a low seed photon temperature was required to reproduce a soft excess at energies $\lesssim 4$ keV, where we chose very small systematic errors, thus making the trend extremely statistically significant. As seen from Fig. 14, however, *fractionally* this trend is subtle and small, and therefore we cannot use the Crab ratios to rule out the possibility of a systematic trend in the (time-dependent) *PCA* response matrices that we use.

One argument in favor of these features *not* being systematic is that the transition to the hard state coincides with the turn on of the radio emission, which initially appears in observation P40108_03 with a mildly optically thin radio spectrum and large amplitude (tens of percent) variations on $\gtrsim 10$ minute time scales (Corbel et al. 2000). It is tempting to associate the unusual soft excess/low fitted seed photon temperatures with the initial formation of the radio outflow.

5.3 Is the ‘ Γ - $\Omega/2\pi$ Correlation’ Real?

As discussed above, the Crab ratios clearly show that the GX 339–4 hard state spectra can be well-described by a broken power law plus a broad line, with the low energy (softer) power law varying more than the high energy (harder) power law (Wilms et al. 1999). Using more physical models, this effect can be found again in the relation between the reflection fraction and the slope of the underlying power law (Zdziarski et al. 1998). Since the shape of the spectrum above 10 keV changes only slightly while the soft spectral index shows a

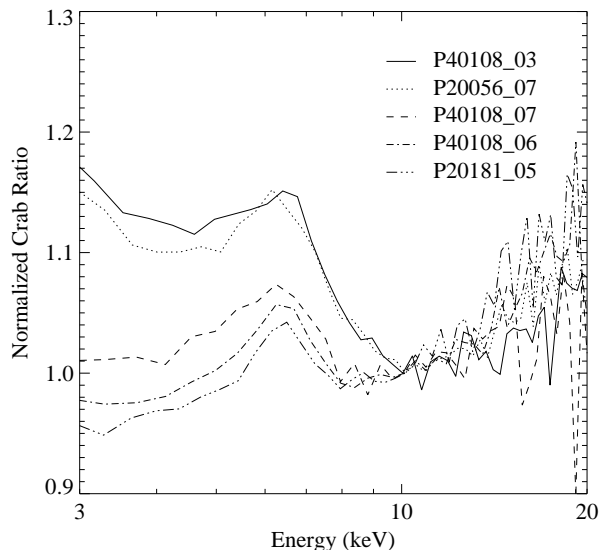


Figure 14. The normalized Crab ratio for observations P20056_07 and P20181_05 with respect to the Crab observation of 1997 September 5, and for observations P40108_03 and P40108_06 with respect to the Crab observation of 1999 February 24. See text for a complete description.

strong variation, the comparably constant spectrum above 10 keV is reproduced by having a stronger reflection component for brighter/softer spectra. This ability of a reflected component to phenomenologically harden a soft power law has caused some, including ourselves (Wilms et al. 1999), to question the reality of the putative Γ - $\Omega/2\pi$ correlation. The Crab ratios, however, remove any doubt. *Viewed from the purely phenomenological perspective of a broken power law model, the ‘ Γ - $\Omega/2\pi$ correlation’ is real.*[§]

Viewed from a physical perspective, the exact nature of these two power law components is still uncertain. As measured with the *Oriented Scintillation Spectrometer Experiment* (OSSE) on board the *Compton Gamma Ray Observatory* (CGRO), the high energy spectrum of GX 339–4 is very well fit by an exponentially cut-off power law, without any additional reflected component (Grove et al. 1998). *HEXTE* spectra fitted by themselves yield very similar results (Wilms et al. 1999). Reflection models are *not* detecting any characteristic “spectral curvature” in the 30–100 keV band. Instead, the reflection models are primarily sensing the break between the low and high energy power laws, with a larger break requiring a greater reflection fraction.

Even here, the exact value of the “reflection fraction” is subject to much uncertainty. As we first discussed for Cyg X-1 (Dove et al. 1998), since its $\gtrsim 10$ keV spectra can be well-described by a spectrum *without* reflection, the fitted reflection fraction is strongly dependent upon one’s assumptions about the nature of the $\lesssim 10$ keV spectrum. For Cyg X-1, we saw that if we allowed a large equivalent width and broad

Fe line, and a higher effective temperature than ‘usual’ soft excess, no reflection was required (again, using earlier versions of the *PCA* responses matrices). On the other hand, the *kotelp* model, which does have an effective reflection fraction of $\Omega/2\pi \approx 0.3$, also fit those data. This is similar to the situation here, where the fits of GX 339–4 discussed in §2.3— which allowed for high temperature seed photons and large equivalent width, broad lines— yielded systematically different “reflection fractions” than the fits of §2.5. The same, physically realistic Comptonization model, which self-consistently calculates the Comptonized spectrum from the seed photon spectrum and coronal parameters, yields different, nearly equally as good, answers for different sets of starting values. Thus, it is very difficult to uniquely determine the ‘best’ continuum model and thereby obtain the most ‘accurate’ value for the reflection fraction (cf. di Salvo et al. 2001).

Again, however, viewed purely from the phenomenological perspective of a broken power law, the *relative* trends are giving us information concerning the degree of the break between the low and high energy power laws. As shown in Fig. 14, those observations that show little or no break in the power law also yield fitted reflection fractions close to zero. This is even given the fact that the Fe line, which may or may not be related to the same component that causes the ‘reflection’, does not vanish.

Fig. 14 also provides an explanation for one of the other results discussed by Wilms et al. (1999). Specifically, Wilms et al. (1999) showed that the P20181 observations discussed here could be fit by an ionized reflector model with a weak and narrow Fe line. The Γ - $\Omega/2\pi$ correlation was absent, but a hardness-ionization parameter correlation was instead detected: softer spectra showed a more highly ionized reflector. Fitting a continuum model consisting of a soft excess (modelled as a 250 eV maximum temperature disc blackbody), and a power law *fitting predominantly the 4–7 keV data*, the power law break can then be viewed as an edge, with the

[§] Note that the soft state *PCA* spectra presented in §4 can also be reasonably well represented by the same models used in Table 5 of Wilms et al. (1999); i.e., a weak disc blackbody with peak temperature ~ 250 eV, a gaussian line, and a broken power law. For those observations, however, the Fe line has an equivalent width ≈ 1.5 keV, and the broken power law indices are ≈ 4.4 , 2.2 for the lower and higher energy power laws, respectively.

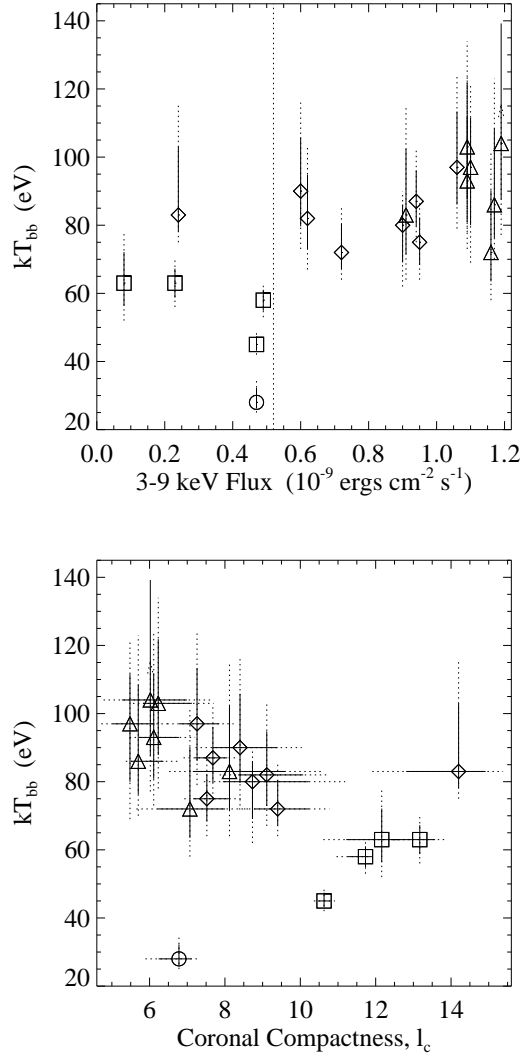


Figure 15. *Top:* Seed photon temperature vs. 3–9 keV *PCA* flux, for the **eqpair** models. *Bottom:* Seed photon temperature vs. coronal compactness, for the **eqpair** models.

position of the edge shifting to higher energies (as would be appropriate for a more ionized reflector) for softer spectra, as is apparent in Fig. 14. Such models quite acceptably describe the data, and in fact can also be shown to describe the P20056 observations as well. Again, we see that given the poor spectral resolution of *RXTE* coupled with the inherent degeneracies of the spectral models (themselves consisting of broad, overlapping components), it is difficult to obtain a unique interpretation of the observed features.

5.4 A (Too?) Simple Coronal Model

In §3, we found that for the **kotelp** model fits the characteristic PSD frequencies scaled approximately $\propto \ell_c^{-3/2}$. Here we provide a simple hypothesis for this behaviour. The **kotelp** model fits a relative compactness of the corona as compared to that of the disc. Let us assume that the transition radius between the disc and the corona occurs at a radius of R_t , while the bulk of the energy release from the corona is

due to falling through the gravitational potential drop to the marginally stable orbit at R_m . The compactness of the corona is proportional to the energy release in the corona divided by the coronal radius, i.e. $\propto R_m R_t^{-1}$. The *intrinsic* compactness of the disc, on the other hand, goes as its gravitational energy release ($\propto R_t^{-1}$) divided by its characteristic radius (R_t) and thus scales as $\propto R_t^{-2}$. The *relative* compactness of corona to disc is therefore $\ell_c \propto R_t/R_m$. This is essentially what we fit with the **kotelp** model.

The fits of §2.4 showed that ℓ_c ranged from ≈ 1 (for the observation after GX 339–4 returned to the hard state in 1999), to ≈ 7 for some of the faintest observations. In the above simple model, the flux-hardness anti-correlation then can be ascribed to the corona-disc transition radius varying from $R_t \approx R_m$ to $R_t \approx 7 R_m \lesssim 40 GM/c^2$, while the accretion rate drops by a factor of $\gtrsim 4$ (assuming that the 3–200 keV flux is a fair measure of the bolometric flux).

If we take the view point of Psaltis & Norman (2000) that the observed PSD is made up of resonant time scales

from the corona-disc transition region, many of these characteristic frequencies scale as $R_t^{-3/2}$ and therefore should scale as $\ell_c^{-3/2}$ in the above scenario, consistent with the results shown in Fig. 9. One implicit assumption made here is that the accretion rate, \dot{M} , scales out of the ratio between the coronal and disc compactness. That is, we are assuming an efficient accretion disc. A further assumption is that the scaling of the frequencies is indeed $\propto R_t^{-3/2}$. Whereas this is true for the dynamical, thermal (for fixed α), vertical epicyclic, and radial epicyclic (for $R \gg 8 GM/c^2$) frequencies, this is not true for the Lense-Thirring precession or viscous damping frequencies.

Although the distance, absolute luminosity, and mass of GX 339–4 are not well-known (see Zdziarski et al. 1998 for a thorough discussion of these points), it has $L \lesssim 5\% L_{\text{Edd}}$ if its fractional Eddington luminosity is comparable to other hard state GBHC (Nowak 1995, and references therein). Thus, in any thin disc Shakura-Sunyaev model, whether it is gas or radiation pressure-dominated, one expects the viscous time scale to be several thousand seconds at $R \sim 20 GM/c^2$, even for α relatively large. This is substantially longer than the low-frequency cutoff time scales presented in Fig. 9. In addition, the ratio between the viscous time scale and the thermal time scale is approximately $\propto (L/L_{\text{Edd}})^{-2} \gtrsim 400$, which is a larger dynamic range than that presented in Fig. 9. Let us assume, however, that the transition region between a corona and disc is *fixed* and is relatively a large fraction of the transition radius, on the order of $H/R \sim 0.1$ – 0.3 . The dynamic range of frequencies shown in Fig. 9 then can be consistent with including the viscous time scale, and furthermore the viscous frequency would also scale as $R_t^{-3/2}$.

Within this simple model, compactness changes are achieved solely by varying the coronal radius, and not by changing the underlying geometry. This is in contrast to the suggestion of Zdziarski, Lubinski, & Smith (1999), who hypothesize that the hardness *and* reflection fraction are regulated by the degree of ‘overlap’ between the cold disc and quasi-spherical corona (more overlap yields both softer spectra and greater reflection fraction). We had previously suggested (Dove et al. 1998) that some amount of overlap was required to produce the broad, large equivalent width line that was required for **kotelp** models of both Cyg X-1 and GX 339–4. We have attempted such simulations with the **kotelp** code; however, our results indicate that the coronal region overlapping the disc cools to the inverse Compton temperature, $kT_{\text{IC}} \approx 4 \text{ keV}$, and thus fails to yield the required additional reflection. *This does not mean such models are ruled out, rather that one needs to carefully model additional, substantial heating in the overlap region in order to maintain the local coronal temperature.* It has been suggested that such local heating can arise from thermal conduction between the corona and disc (Meyer & Meyer-Hofmeister 1994), although it has not been rigorously shown that such heating is sufficient.

The above ‘overlap’ model has been suggested as possibly being applicable to an overall ‘ Γ - $\Omega/2\pi$ correlation’ common to Seyfert 1 galaxies and galactic black hole candidates (Zdziarski et al. 1999). However, as discussed above, the viscous time scale in a thin, low luminosity accretion disc about a low mass black hole is hundreds to thousands of seconds. Thus, each *individual* observation discussed here is integrated over many viscous time scales, while different

observations can, and likely do, represent vastly different intrinsic accretion rates through the disc. This is in contrast to a $10^8 M_\odot$ black hole in a Seyfert 1 (e.g., NGC 5548; see Chiang et al. 2000, and references therein), which likely has a characteristic viscous time scale of *years*. The week to week spectral variations of NGC 5548 discussed by Chiang et al. (2001) therefore correspond to thermal time scales and faster. Such thermal time scales are integrated over in a few seconds in our observations of GX 339–4. Thus, whereas their are undoubtedly commonalities between Seyfert 1’s and GBHC, it would be surprising if the exact same models were responsible for the spectral correlations seen in both.

A major failure of the above simple model is that it does not explain the putative reflection fraction correlation with compactness. To consider this further, we turn to the **eqpair** model results, which do allow for reflection changes. The **eqpair** model fits agree in rough outline, but not in detail, with the **kotelp** model fits. Specifically, both require coronal temperatures $\gtrsim 150 \text{ keV}$ (although **eqpair** fits tend to have optical depths lower by a factor of approximately 2–3), and both are consistent with overall low reflection fractions of $\Omega/2\pi \lesssim 0.5$. This reflection fraction, however, is clearly variable in the **eqpair** fits. In addition, the **eqpair** model also requires a seed photon temperature variation, which in turn relates to the “effective coronal radius” for these models. Since we have fixed the seed photon compactness to one, the fitted **eqpair** coronal compactness scales as $F_{\text{bol}}/(\sigma_{\text{SB}} T_{\text{bb}}^4 R_\gamma^2)$, where F_{bol} is the bolometric flux, σ_{SB} is the Stefan-Boltzman constant, T_{bb} is the temperature of the seed photons, and R_γ is the “effective radius” for the seed photon distribution, which for the **eqpair** model is assumed to be on the order of the coronal radius. Assuming that the 3–200 keV flux is a fair measure of the bolometric flux, and taking a distance of 4 kpc and a mass of $4 M_\odot$ for GX 339–4, this effective radius, in units of GM/c^2 , is approximately

$$60 \left(\frac{d}{4 \text{ kpc}} \right) \left(\frac{4 M_\odot}{M} \right) \left(\frac{100 \text{ eV}}{kT_\gamma} \right)^2 \left(\frac{F_{\text{bol}}}{10^{-9} \frac{\text{erg}}{\text{cm}^2 \text{ s}}} \right) \ell_c^{-\frac{1}{2}}. \quad (3)$$

We plot characteristic PSD frequencies vs. this radius in Fig. 16.

Note that in the hysteretic/overlap region (the brightest seven P20181 observations), the effective radius and frequencies are roughly constant and, within the large uncertainties, $\lesssim 100 GM/c^2$. However, for the 1999 return to the hard state, the radius trends are exactly *opposite* of those implied by the **kotelp** fits. Specifically, the effective radius is seen to be very large, and then shrinks. This behaviour, although counter to an association of the PSD *frequencies* with a coronal radius, is in agreement with the association of the *time lags* with a characteristic size scale, as we also show in Fig. 16. Is this necessarily in contradiction to the **kotelp** results?

For the 1999 hard state observations, the large reduced χ^2 ’s achieved for most of the **kotelp** models were primarily due to residuals in the 3–4 keV band (with some contribution from an “edge-like” residual near 10 keV). Otherwise, the **kotelp** models fit the data reasonably well, especially at high energies. The low seed photon temperatures found with the **eqpair** model were largely driven by the 3–4 keV residuals. We speculate here that the “true” model might be a combination of the suggested compactness/frequency/time-lag/radii relations above. That is, perhaps the correct model

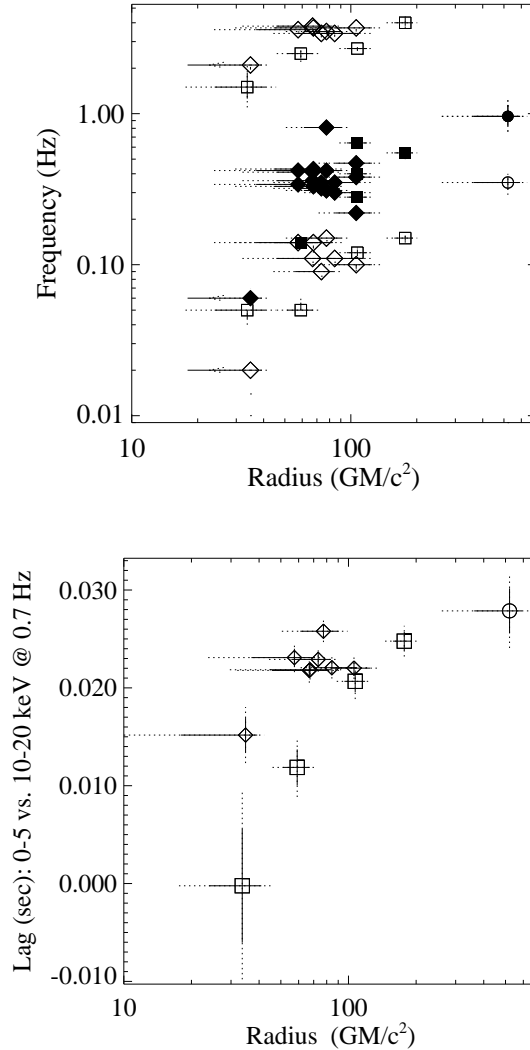


Figure 16. *Top:* Characteristic PSD frequencies vs. “effective radius” for the seed photon distribution from the **eqpair** fits. *Bottom:* Time lags between soft and hard variability (average PSD frequency 0.7 Hz) vs. effective radius from the **eqpair** fits. For clarity, only the higher signal-to-noise P20181 and P40108 observations are shown.

involves the radii of the *base* of the corona increasing with decreasing flux/increasing compactness, while the *vertical* extent of the corona decreases for decreasing flux/increasing compactness. The initial transition to the hard state, exhibited by observation P40108_03, could be associated with the formation of a large vertical scale jet, with X-ray emission extending to nearly $1000 \text{ GM}/c^2$, while its base has a radius on the order of the marginally stable orbit. The characteristic PSD frequencies could then be generated within the disc, while the characteristic time lags could be generated via propagation along the length of the jet. An extended jet would also “view” a much larger extent of the disc, and thereby have a greater reflection fraction. (The slightly low reflection fraction exhibited by observation P40108_03 given its long time lag, as seen in Fig. 12, might also be attributed to some amount of beaming away from the disc, as suggested, e.g., by Beloborodov 1999.) The reflection fraction

would naturally decrease as the jet height decreases and the jet base widens.

Clearly the above suggestion requires detailed theoretical modelling to verify. Furthermore, it is subject to great observational uncertainty. Specifically, are the seed photon temperature trends shown in Fig. 15 real or systematic errors? However, we note that the large effective radius implied by the **eqpair** fit to observation P40108_03 implies the possibility for this observation, and the subsequent two observations, of having a large contribution from *synchrotron* seed photons, as opposed to solely thermal seed photons. Taking the fitted **eqpair** coronal temperature and optical depths, and hypothesizing a magnetic field in equipartition with the thermal energy of the corona, then the expected flux (at 4 kpc, assuming a $4 M_\odot$ black hole) due to synchrotron emission within the corona is on the order of

$$F_{\text{sync}} \sim 3 \times 10^{-12} \text{ ergs}^{-1} \text{ cm}^{-2} \left(\frac{R_c}{\text{GM}/c^2} \right) \left(\frac{kT_c}{200 \text{ keV}} \right)^2 \left(\frac{\tau_{\text{es}}}{0.3} \right)^2. \quad (4)$$

Given a typical bolometric flux of $10^{-8} \text{ erg s}^{-1} \text{ cm}^{-2}$ and an implied “seed photon” flux of $\approx 10^{-9} \text{ erg s}^{-1} \text{ cm}^{-2}$, we see that the synchrotron flux only becomes comparable to the thermal seed photon flux for an effective coronal radius $\gtrsim 300 \text{ GM}/c^2$, i.e. the implied effective radius of observation P40108_03. Again, this observation, coincident with the initial transition to the hard state, showed unusually large radio variability on 10 minute time scales, as well as exhibited a quasi-optically thin radio spectrum (Corbel et al. 2000). Thus, the low fitted seed photon temperature for the **eqpair** model may have been indicating the need to consider synchrotron seed photons.

5.5 Implications for ADAFs

An Advection Dominated Accretion Flow was first suggested as a model for the hard state spectrum of Cyg X-1 by Ichimaru (1977). Since that time, there has been much further research and applications to spectra of GBHC. One of the key questions in applying ADAF models has been, where is the transition between the hot, geometrically thick advective flow and the cool, geometrically thin outer disc located? Esin, McClintock, & Narayan (1997) had originally proposed that the soft to hard state change in GBHC was associated with an increase of the “transition radius” from $\approx 10 \text{ GM}/c^2$ to $\approx 10^4 \text{ GM}/c^2$. Esin et al. (1998) later revised this range, for models of Cyg X-1, to $\approx 60 \rightarrow 400 \text{ GM}/c^2$. Recent models of XTE J1118+480 require the transition radius to be $\gtrsim 100 \text{ GM}/c^2$ (Esin et al. 2001).

This aspect of the ADAF model can be tested with these observations. We see that for both the **kotelp** and **eqpair** models, with the exception of the first few observations after the 1999 return to the hard state, the implied coronal radii are all $\lesssim 100 \text{ GM}/c^2$. There is no evidence for *large amplitude* variations in this radius as the observed flux decreases (di Matteo & Psaltis 1999). In fact, both the **eqpair** and **kotelp** models suggest that for the faintest observation, P40108_07, which is 15 times fainter than the brightest hard state and 5 times fainter than the initial transition back to the hard state in 1999, that the effective coronal radius has actually shrunk in comparison to the previous hard state observations at higher fluxes.

Evidence for a small coronal radius for observation P40108_07 also comes from the observed Fe line, which in Fig. 14 clearly exhibits a broad, red tail. Fitting the 3–20 keV PCA data of this observation with a combination of a power law and a relativistic **diskline** model (Fabian et al. 1989), we find the following limits on the *inner* radius of this emission. Assuming a line at 6.4 keV, with a 45° inclination for the disc, and a line emissivity that is $\propto R^{-3}$, the best fit inner radius is $14_{-8}^{+93} \text{ GM}/c^2$ (90% confidence level). Replacing the power law with a power law plus reflection (i.e., Magdziarz & Zdziarski 1995; here with a best fit value of $\Omega/2\pi = 0.2$), we find an inner disc radius of $6_{-0}^{+16} \text{ GM}/c^2$. Replacing the reflected power law with an **eqpair** model as in §2.5, the inner disc radius is $13_{-7}^{+34} \text{ GM}/c^2$. Such small implied inner disc radii are strongly counter to what would be the best evidence for the “typical” ADAF model.

Of course, it is possible that the advection dominated region only exists at radii $\lesssim 100 \text{ GM}/c^2$. The arguments presented above about the scaling of the PSD time scales with the **kotelp** compactness parameter, which assumed efficient

accretion, are only very weak, indirect evidence against advection domination. However, none of the observations here require advection domination either, and there is no compelling evidence for any efficiency change from the soft to hard state spectra. The observations are all consistent with the spectral changes solely being determined by accretion rate changes. (Further evidence of this comes from the fact that the radio flux closely *linearly* tracks the X-ray flux, all the way into quiescence; Corbel et al. 2001, in preparation.)

5.6 Alternative Models?

As shown in Fig. 17, some of our observations (most notably P20181_01) exhibit a hardening above $\sim 100 \text{ keV}$ in the **HEXTE** data. One possible explanation would be that the hardening is hinting at presence of a high-energy power-law tail as seen, e.g., in Cyg X-1 (McConnell et al. 2000). Power-law tails are generally attributed to the presence of a non-thermal electron population in the Comptonizing plasma (Bednarek et al. 1990; Gierliński et al. 1997; Coppi 1999). Alternatively, weak power-law tails have also been explained in terms of thermal Comptonization in a Maxwellian plasma with a temperature gradient (Skibo & Dermer 1995). In these models, the temperature gradient serves to make the “effective” electron distribution non-thermal. See McConnell et al. (2000) for a discussion of these mechanisms. In galactic black holes, power-law tails are generally associated with the soft state or with transitions into the soft state. As these transitions are typically associated with enhanced radio emission (Fender 2000), one is tempted to see the presence of the power-law tail as an indication of the non-thermal electron distribution in a radio outflow (Markoff et al. 2001).

A possible alternative explanation for the power-law tail, however, is that it is due to instrumental effects: The tail could also be due to an incomplete background subtraction that might be caused either by the uncertainty in the estimation of the **HEXTE** live-time or by a transient background source. Such checks are especially important since the **HEXTE** background contains two strong line complexes below 100 keV. In order to test for the presence of a background source we extracted individual **HEXTE** background spectra for each of the two background dwells of the **HEXTE** clusters and then compared these spectra to each other. In the case of observation P20181_01, the difference between the plus and minus background position for cluster B is $3.6 \times 10^{-2} \text{ cps}$, consistent with statistical fluctuations. On the other hand, for cluster A the difference between the two background dwells amounts to almost 1 cps. The difference spectrum between the two dwells, however, does not resemble the observed hardening in GX 339–4. Furthermore, we note that we see the tail in both **HEXTE** clusters which makes it quite improbable that this 1 cps difference is the cause of the hard tail. We conclude that the question of the hard tail in GX 339–4 is still open for discussion, but that its association with a problem of the background subtraction is not strongly suggested. Observations with more sensitive gamma-ray detectors are needed to determine whether this tail is a real feature.

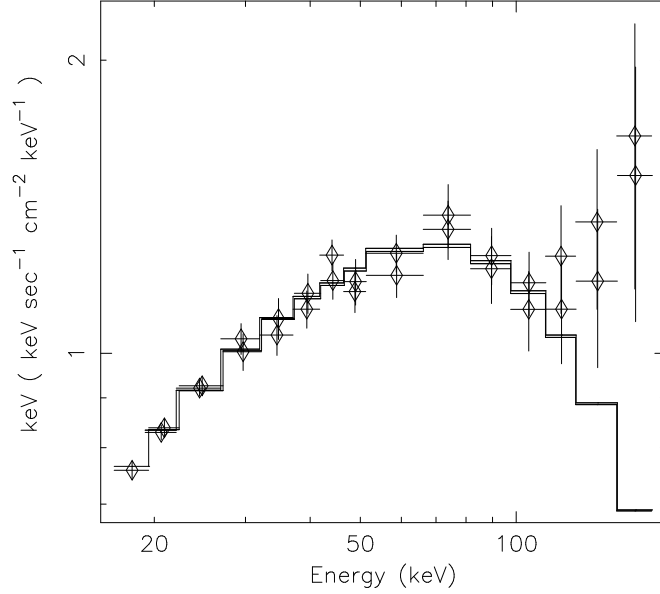


Figure 17. The unfolded *HEXTE* spectrum of observation P20181_01. The data have been fit with a *kotelp* model.

6 SUMMARY

We have presented spectral and timing analysis of 22 individual observations of the galactic black hole candidate GX 339–4, as observed by the *Rossi X-ray Timing Explorer*. Several of these observations were coincident with *Advanced Satellite for Cosmology and Astrophysics*, radio, and/or optical observations. Our chief results for the X-ray analyses are as follows.

- As has been previously observed, the soft state has a strong soft excess below ≈ 7 keV, a weak hard tail, and very little X-ray variability. Also in agreement with previous observations, the hard state, although exhibiting a spectral break at ≈ 10 keV, does not show a strong soft excess, does have a strong hard energy tail, and exhibits large amplitude, rapid X-ray variability.

- Generally, the hard state exists at lower bolometric luminosities than the soft state; however, in terms of 3–9 keV flux, there appears to be a “hysteresis” in the state transitions, as first discussed by (Miyamoto et al. 1995). The degree of this hysteresis in terms of the bolometric flux is unclear.

- Brighter flux states tend to show softer overall spectra; however, the first few observations after the 1999 return to the hard state are unusually soft. (This is the first “return” to a hard state observed by *RXTE* in GX 339–4.) In addition, we have discovered that the trend of hardening spectra with decreasing flux is broken for the lowest flux observation.

- Both the soft state and hard state spectra can be reasonably well represented by Comptonization models, with parameters similar to previous analyses. However, there is a great deal of degeneracy in these models, with different models producing comparable fits. The *kotelp* and *eqpair* hard state models both require coronal temperatures $\gtrsim 100$ keV and both are consistent with reflection fractions $\Omega/2\pi \lesssim 0.5$; however, the former requires an approximately factor of three greater optical depth. In addition, there are basic differences between these models (e.g., 100% of the seed pho-

tons pass through the corona in the *eqpair* model, whereas $\approx 30\%$ of the seed photons pass through the corona in the *kotelp* model).

- The hard state spectra show a break at ≈ 10 keV, with the spectrum hardening at higher energies. Modelling this as a broken power law, the degree of this break increases with brighter/softer spectra. This has been dubbed the ‘ Γ - $\Omega/2\pi$ correlation’ in previous analyses with reflection models. Within the context of reflection models, in contrast to previous analyses, we find that the “reflection fraction” is better correlated with 3–9 keV flux than with the spectral hardness.

- Most models require the presence of a broad, large equivalent width Fe line. For the 1997 hard state, the equivalent width of this line is correlated with the reflection fraction. For the 1999 hard state, unlike for previous observations, the line remains broad and at relatively constant equivalent width, even into quiescence. This is counter to the simplest expectations of ADAF models. Ratios of the GX 339–4 data to observations of the Crab nebula and pulsar show that these results represent real effects, and not systematic errors.

- Timing analysis shows that brighter, softer spectra tend to have higher characteristic PSD frequencies than fainter, harder spectra, as has been previously observed in both GX 339–4 and Cyg X-1. We have, however, included more variability components than previous analyses, and furthermore we have correlated our results with coronal parameters, rather than a power-law index. We here have discovered also that the variability time lags show the opposite trends from the PSD frequencies. Bright, soft spectra tend to show the longest time lag of the hard X-ray variability behind the soft X-ray variability.

- A correlation between time lag and ‘reflection fraction’ was also newly discovered. The longest time lag was seen for the first observation taken after the 1999 return to the hard state, similar to observations of ‘failed state transitions’ in Cyg X-1 (Pottschmidt et al. 2000). The 1999 return of

GX 339–4 to its hard state also exhibited unusual radio properties.

- Variability properties, both for the characteristic PSD frequencies and measured time lags, were most uniform in the “hysteretic” range of 3–9 keV fluxes (cf. Revnivtsev, Gilfanov, & Churazov 2001).

- We have hypothesized that a radiatively efficient corona, wherein the base of the corona/jet decreases and its height increases, with increasing flux/softness, might be able to explain a number of the observed spectral-variability correlations.

- More speculatively (due to uncertainties in instrument backgrounds and calibration), there is new evidence within the brightest, softest observations for a power law extending beyond the spectral roll-over usually associated with thermal Comptonization. The first few observations after the 1999 return to the hard state also exhibited an unusual soft excess, which we speculated might be related to the turn on of the radio jet.

Our own inclination is to believe that the hard tail observed for observation P20181_01 and that the soft excesses observed for observations P40108_03–05 represent real phenomena, and not systematic effects. Their full implications can only be addressed with improved observations. For the former, there is some hope that *Integral* will provide refined high energy observations. For the latter, simultaneous *XMM-Newton*/*RXTE* or *Chandra*/*RXTE* observations will be crucial for describing the seed photon regime of the spectra. This will be especially important, for example, in breaking the degeneracy between the 600 eV seed photon/50 keV corona fits (§2.3) and the 100 eV seed photon/150 keV corona fits (§2.5) given by the **eqpair** models. Furthermore, the ratio of the Comptonized flux to the seed photon flux (e.g., the “amplification factor”) has implications for the coronal geometry. In this sense, the **eqpair** and **kotelp** models are very different, and in fact, the optical (seed photon) to X-ray (Comptonized) flux might be constraining Seyfert 1 geometries in this manner (Chiang & Blaes 2001; in preparation). Finally, none of the currently available Comptonization models are truly adequate for describing these data. Theoretical work, accounting for jet-like geometries and the presence of the *known* radio emitting outflow need to be more fully explored.

This research has been supported partially by NASA grant NAG5-3225 (MAN). We would like to acknowledge useful conversations with C. Bailyn, J. Chiang, P. Coppi, S. Corbel, R. Fender, R. Jain, T. Maccarone, C. Reynolds, and R. Soria. M.A.N. would like to thank the Yale Dept. of Astronomy, where much of this work was performed, for their hospitality. This research has made use of data obtained through the High Energy Astrophysics Science Archive Research Center Online Service, provided by the NASA/Goddard Space Flight Center.

APPENDIX A: DATA ANALYSIS METHODS

A1 RXTE Data Analysis

All *RXTE* results in this paper were obtained using the standard *RXTE* data analysis software, **ftools** version 5.0 with

the corresponding *PCA* response matrix, and *HEXTE* response matrix dated 97mar20c. Data selection criteria were that the source elevation was larger than 10° above the earth limb and data measured within 30 minutes of passages of the South Atlantic Anomaly or during times of high particle background (as expressed by the “electron ratio” being greater than 0.1) were ignored. For one archival observation, P20056_04, these criteria produced only 45 sec of usable data, in contrast to the discussion of this observation found in Revnivtsev, Gilfanov, & Churazov (2001). Analysis of archival Crab observations indicated that low residual, uniform results (in terms of measured spectral slope of the Crab from observation to observation) were best achieved by restricting the analysis to the first anode layer of the proportional counter units (PCUs). We therefore only consider this top layer throughout this work. For both spectral and timing analyses, we combined the data from all active PCUs (typically four or five PCUs were active at any given time).

For spectral fitting, we limited the energy range of the *PCA* data from 3 to 22 keV and the energy range of the *HEXTE* from 19 to 198 keV. *PCA* channels were grouped so that each had a minimum of 20 counts, while *HEXTE* channels were grouped by: a factor of 3 for channels 16–20, a factor of 5 for channels 22–51, a factor of 15 for channels 52–126, and a factor of 24 for channels 127–198. To take into account the calibration uncertainty of the *PCA* we applied channel dependent systematic uncertainties in a manner similar to that described by Wilms et al. (1999). These uncertainties were determined from a power-law fit to observations of the Crab nebula and pulsar. As described on the *RXTE* Guest Observer Facility web pages, the high voltage gain of the *PCA* detectors was changed in mid-March 1999 (demarking the change from *PCA* ‘Gain Epoch 3’ to ‘Gain Epoch 4’). For all the P20181 and P20056 observations, as well as observations P40108_01–04 (‘Epoch 3’), we applied 0.3% systematic errors in *PCA* channels 0–10, 1% systematic errors in channels 11–18, 0.5% systematic errors in channels 19–29, 1% systematic errors in channels 30–51, and 2% systematic errors in channels 52–128. For observations P40108_05–07 (‘Epoch 4’), these same systematic errors were applied instead to *PCA* channels 0–8, 9–15, 16–24, 25–43, and 44–128, respectively. Background subtraction of the *PCA* data was performed using the ‘SkyVLE’ model, as for our previous studies of GX 339–4 (Wilms et al. 1999).

As discussed by Wilms et al. (1999), there is a systematic difference between the *PCA* and the *HEXTE* detectors for the best fit photon index for observations of the Crab nebula and pulsar. *PCA* fits yield a Crab photon index of $\Gamma = 2.18$, while *HEXTE* fits yield $\Gamma = 2.08$. We have made no attempt to account for any slope differences; however, we have accounted for the cross-calibration normalization uncertainties of the *PCA* and the *HEXTE* instruments relative to each other by introducing a multiplicative constant for each detector in all of our fits. Typically, if the *PCA* constant was fixed at 1, the multiplicative constants were ≈ 0.9 for the *HEXTE* A cluster, and a few percent lower for the *HEXTE* B cluster.

In all of our spectral fits, we have modelled the neutral hydrogen column using the cross sections of Morrison & McCammon (1983). Furthermore, unless otherwise noted, we have fixed the value for GX 339–4 to $6 \times 10^{-21} \text{ cm}^{-2}$. In the parameter tables below, italicized parameter values

indicate that the parameter was frozen at that value for that analysis.

For the variability analyses, we follow the methods of Nowak et al. (1999a), and references therein. Throughout this work we have adopted the PSD normalization of Belloni & Hasinger (1990), where integrating over positive Fourier frequencies yields the root mean square (rms) variability of the lightcurve. We created lightcurves with a time resolution of 2^{-8} sec; therefore, the Nyquist frequency was 128 Hz for all observations. For the PSD fits discussed above, however, we fit the data from 3×10^{-3} Hz to an upper cutoff frequency, which is listed in Table A4 and Table A5 for each observation. Furthermore, we logarithmically binned each PSD over a range of Fourier frequencies, $\Delta f/f$, that varied between 0.06–0.15, depending upon the statistics of each observation.

We performed variability analysis between two energy bands: 0–5 keV and 10–20 keV. These energy bands corresponded to PCA pha channels 0–13 and 27–53 for the P20181 observations and for observations P40108_03_04, and to PCA pha channels 0–10 and 22–44 for observations P40108_05_07. The P20056 observations used a data mode with very limited high energy resolution, therefore the high energy band for those observations corresponds to 10–100 keV, i.e., PCA pha channels 26–249. Since this is such a broad range, which includes many noise dominated channels, we did not calculate the time lags for the P20056 observations.

A2 ASCA Data Extraction

We extracted data from the two solid state detectors (*SIS0*, *SIS1*) and the two gas detectors (*GIS2*, *GIS3*) on board ASCA by using the standard ftools as described in the ASCA Data Reduction Guide (Day et al. 1998). We chose circular extraction regions with radii of ≈ 4 arcmin for the *SIS* detectors, and ≈ 6 arcmin for the *GIS* detectors. We excluded approximately the central 1 arcmin of the *SIS* detectors to avoid the possibility of photon pile-up. We used the *sisclean* and *gisclean* tools (with default values) to remove hot and flickering pixels. We filtered the data with the strict cleaning criteria outlined by Brandt et al. (1996); however, we took the larger value of 7 GeV/c for the rigidity. The background was measured from rectangular regions on the two edges of the chip farthest from the source (*SIS* data), or from annuli with inner radii > 6 arcmin (*GIS* data). These data were cleaned and filtered in the same manner as the source files.

We combined the two *SIS* detectors into a single spectrum, and we combined the two *GIS* detectors into a single spectrum, properly weighting the response matrices and backgrounds. Furthermore, we rebinned the spectral files as follows. For the *SIS* spectra, the channels were grouped: by a factor of 5 for channels 17–246, by a factor of 10 for channels 247–266, by a factor of 15 for channels 267–311, by a factor of 20 for channels 312–351, and by a factor of 29 for channels 352–380. For the *GIS* spectra, the channels were grouped: by a factor of 10 for channels 18–617, by a factor of 15 for channels 618–752, by a factor of 30 for channels 753–932, and by a factor of 39 for channels 933–971. Note that these observations were taken rather late in the lifetime of ASCA, after the *SIS* detectors in particular had sustained heavy radiation damage. Although the *SIS* and *GIS* detectors were

in good agreement with one another from 1.8–10 keV, they were noticeably different from one another in the 1–1.8 keV range. (The *GIS* spectra were systematically softer than the *SIS* spectra in this energy range.) Taking this as possibly due to *SIS* radiation damage, we only considered *SIS* data in the 2–10 keV band, whereas we considered *GIS* data in the 1–10 keV band.

We accounted for the cross-calibration uncertainties of the *SIS* and *GIS* instruments relative to each other and relative to *RXTE* by introducing a multiplicative constant for each detector in all of our fits. Note that, relative to observations of the Crab nebula and pulsar, *ASCA* fluxes are systematically lower than *RXTE* fluxes by $\approx 80\%$, which we have confirmed with our simultaneous *ASCA/RXTE* observations. Throughout this work we always quote *PCA* fluxes; however, this needs to be borne in mind when comparing the flux levels discussed here to the *ASCA* flux levels presented in Table 1 of Wilms et al. (1999).

REFERENCES

- Arnaud K. A., 1996, in Jacoby J. H., Barnes J., eds, *Astron. Soc. Pacific, Conf. Ser.* 101, *Astronomical Data Analysis Software and Systems V*. Astron. Soc. Pacific, San Francisco, p. 17
- Balbus S. A., Hawley J. F., 1991, *ApJ*, 376, 214
- Bednarek W., Karakula S., Tkaczyk W., Giovannelli F., 1990, *A&A*, 236, 175
- Belloni T., Hasinger G., 1990, *A&A*, 227, L33
- Belloni T., Méndez M., van der Klis M., Lewin W. H. G., Dieters S., 1999, *ApJ*, 519, L159
- Beloborodov A. M., 1999, *ApJ*, 510, L123
- Brandt W. N., Fabian A. C., Dotani T., Nagase F., Inoue H., Kotani T., Segawa Y., 1996, *MNRAS*, 283, 1071
- Chiang J., Reynolds C. S., Blaes O., Nowak M. A., Murray N., Madejski G., Marshall H., 2001, *ApJ*, 528, 292
- Coppi P., 1999, *PASP Conference Series*, 161, 375
- Corbel S., Fender R. P., Tzioumis A. K., Nowak M., McIntyre V., Durouchoux P., Sood R., 2000, *A&A*, 359, 251
- Day C., Arnaud K., Ebisawa K., Gotthelf E., Ingham J., Mukai K., White N., 1998, *The ASCA Data Reduction Guide*, Technical report, NASA Goddard Space Flight Center, Greenbelt, Md. Version 2.0
- di Matteo T., Psaltis D., 1999, *apj*, 526, L101
- Di Salvo T., Done C., Zycki P. T., Burderi L., Robba N. R., 2001, *ApJ*, 547, 1024
- Done C., 2001, *Adv. Space Res.*, 28, 255
- Done C., Zycki P. T., 1999, *MNRAS*, 305, 457
- Dove J. B., Wilms J., Begelman M. C., 1997a, *ApJ*, 487, 747
- Dove J. B., Wilms J., Maisack M. G., Begelman M. C., 1997b, *ApJ*, 487, 759
- Dove J. B., Wilms J., Nowak M. A., Vaughan B. A., Begelman M. C., 1998, *MNRAS*, 298, 729
- Ebisawa K., 1997, *Adv. Space Res.*, 19, 5
- Esin A. A., McClintock J. E., Drake J. K., Garcia M. R., Haswell C. A., Hynes R. I., Muno M. P., 2001, *ApJ*, 555, 483
- Esin A. A., McClintock J. E., Narayan R., 1997, *ApJ*, 489, 865
- Esin A. A., Narayan R., Cui W., Grove J. E., Zhang S., 1998, *ApJ*, 505, 854
- Fabian A. C., Rees M. J., Stella L., White N., 1989, *MNRAS*, 238, 729
- Fender R. et al., 1999, *ApJ*, 519, L165
- Fender R. P., 2000, in Kaper L., van den Heuvel E. P. J., Woudt P. A., eds, *ESO workshop on Black Holes in Binaries and Galactic Nuclei*. Springer, Heidelberg
- Fender R. P., 2001, *MNRAS*, 322, 31

- Frontera F. et al., 2001, *ApJ*, 546, 1027
- Gierliński M., Zdziarski A. A., Done C., Johnson W. N., Ebisawa K., Ueda Y., Haardt F., Philips B. F., 1997, *MNRAS*, 288, 958
- Gierliński M., Zdziarski A. A., Poutanen J., Coppi P. S., Ebisawa K., Johnson W. N., 1999, *MNRAS*, 309, 496
- Grebenev S. A., Syunyaev R., Pavlinsky M. N., Dekhanov I. A., 1991, *Sov. Astron. Lett.*, 17, 413
- Grove J. E., Johnson W. N., Kroeger R. A., McNaron-Brown K., Philips J. G. S. B. F., 1998, *ApJ*, 500, 899
- Haardt F., Maraschi L., 1993, *ApJ*, 413, 507
- Hannikainen D. C., Hunstead R. W., Campbell-Wilson D., Sood R. K., 1998, *A&A*, 337, 460
- Ichimaru S., 1977, *ApJ*, 214, 840
- Ilovaisky S. A., Chevalier C., Motch C., Chiappetti L., 1986, *A&A*, 164, 671
- Imamura J. N., Kristian J., Middleditch J., Steiman-Cameron T. Y., 1990, *ApJ*, 365, 312
- Kaaret P., Piraino S., Bloser P. F., Ford E. C., Grindlay J. E., Santangelo A., Smale A. P., Zhang W., 1999, *ApJ*, 520, L37
- Kazanas D., Hua X. M., Titarchuk L., 1997, *ApJ*, 480, 280
- Kreykenbohm I., Kretschmar P., Wilms J., Staubert R., Kendziorra E., Gruber D., Rothschild R., 1999, *A&A*, 341, 141
- Laor A., 1991, *ApJ*, 376, L90
- Magdziarz P., Zdziarski A. A., 1995, *MNRAS*, 273, 837
- Maloney P. R., Begelman M. C., 1997, *ApJ*, 491, L43
- Markoff S., Falcke H., Fender R., 2001, *ApJ*, 372, L25
- McConnell M. L. et al., 2000, *ApJ*, 543, 928
- Méndez M., van der Klis M., 1997, *ApJ*, 479, 926
- Meyer F., Meyer-Hofmeister E., 1994, *A&A*, 288, 175
- Mitsuda K. et al., 1984, *PASJ*, 36, 741
- Miyamoto S., Kimura K., Kitamoto S., Dotani T., Ebisawa K., 1991, *ApJ*, 383, 784
- Miyamoto S., Kitamoto S., 1989, *Nature*, 342, 773
- Miyamoto S., Kitamoto S., Iga S., Hayashida K., Egoshi W., 1995, *ApJ*, 442, L13
- Miyamoto S., Kitamoto S., Iga S., Negoro H., Terada K., 1992, *ApJ*, 391, L21
- Morrison R., McCammon D., 1983, *ApJ*, 270, 119
- Nayakshin S., Dove J. B., 2001, *ApJ* submitted (astro-ph/9811059)
- Nayakshin S., Kallman T. R., 2001, *ApJ*, 546, 406
- Nowak M. A., 1995, *PASP*, 107, 1207
- Nowak M. A., 2000, *MNRAS*, 318, 361
- Nowak M. A., Vaughan B. A., Wilms J., Dove J., Begelman M. C., 1999a, *ApJ*, 510, 874
- Nowak M. A., Wilms J., Dove J. B., 1999b, *ApJ*, 517, 355
- Nowak M. A., Wilms J., Heindl W. A., Pottschmidt K., Dove J. B., Begelman M. C., 2001, *MNRAS*, 320, 316
- Nowak M. A., Wilms J., Vaughan B. A., Dove J., Begelman M. C., 1999c, *ApJ*, 515, 726
- Pottschmidt K., Wilms J., Nowak M. A., Heindl W. A., Smith D. M., Staubert R., 2000, *A&A*, 357, L17
- Poutanen J., Fabian A. C., 1999, *MNRAS*, 306, 31p
- Poutanen J., Krolik J. H., Ryde F., 1997a, *MNRAS*, 221, 21p
- Poutanen J., Svensson R., 1996, *ApJ*, 470, 249
- Poutanen J., Svensson R., Stern B., 1997b, in Winkler C., Courvoisier T. J. L., Durouchoux P., eds, *ESA SP 382, The Transparent Universe*. ESA Publications Division, Noordwijk, p.401
- Predehl P., Bräuninger H., Burkert W., Schmitt J. H. M. M., 1991, *A&A*, 246, L40
- Pringle J. E., 1996, *MNRAS*, 281, 357
- Psaltis D., Belloni T., van der Klis M., 1999, *ApJ*, 520, 262
- Psaltis D., Norman C., 2000, *ApJ* submitted (astro-ph/0001391)
- Revnivtsev M., Gilfanov M., Churazov E., 2001, *Reflection and noise in the low spectral state of GX339-4*, *A&A*, in press (astro-ph/9910423)
- Ross R. R., Fabian A. C., 1993, *MNRAS*, 261, 74
- Santangelo A., del Sordo S., Segreto A., dal Fiume D., Orlandini M., Piraino S., 1998, *A&A*, 340, L55
- Shakura N. I., Sunyaev R., 1973, *A&A*, 24, 337
- Shrader C. R., Titarchuk L., 1999, *ApJ*, 521, L121
- Skibo J. G., Dermer C. D., 1995, *ApJ*, 455, L25
- Steiman-Cameron T. Y., Imamura J. N., Middleditch J., Kristian J., 1990, *ApJ*, 359, 197
- Stern B. E., Poutanen J., Svensson R., Sikora M., Begelman M. C., 1995, *ApJ*, L13
- Stone J. M., Hawley J. F., Gammie C. F., Balbus S. A., 1996, *ApJ*, 463, 656
- Sunyaev R. A., Trümper J., 1979, *Nature*, 279, 506
- van der Klis M., Swank J., Zhang W., Jahoda K., Morgan E., Lewin W., Vaughan B., van Paradijs J., 1996, *ApJ*, 469, L1
- Wijnands R., van der Klis M., 1999, *ApJ*, 514, 939
- Wilms J., Nowak M. A., Dove J. B., Fender R. P., di Matteo T., 1999, *ApJ*, 522, 460
- Wilms J., Nowak M. A., Pottschmidt K., Dove W. A. H. J. B., Begelman M. C., 2001, *MNRAS*, 320, 316
- Zdziarski A. A., Lubiński P., Smith D. A., 1999, *MNRAS*, 303, L11
- Zdziarski A. A., Poutanen J., Mikołajewska J., Gierliński M., Ebisawa K., Johnson W. N., 1998, *MNRAS*, 301, 435
- Zhang W., Smale A. P., Strohmayer T. E., Swank J. H., 1998, *ApJ*, 500, L171

A3 Fit Parameter Tables

Table A1. Parameters for models fit to *RXTE* (*PCA*+*HEXTE*) hard state data of GX 339–4. Left: *kotelp*; 72 degrees of freedom (DoF) for P20181_01-P40108_04; 66 DoF for P40108_05–07. Right: *eqpair*; 70 DoF for P20181_01-P40108_04; 64 DoF for P40108_05–07.

Obs.	ℓ_c	τ_{es}	σ_{line} (keV)	EW (eV)	χ^2	ℓ_c	τ_{es} (10^{-2})	kT_{bb} (eV)	$\Omega/2\pi$ (10^{-2})	σ_{line} (keV)	EW (eV)	χ^2
P20181_01	$3.3^{+0.4}_{-0.3}$	$1.2^{+0.2}_{-0.2}$	$0.8^{+0.1}_{-0.1}$	197^{+28}_{-28}	105	$7.3^{+1.0}_{-0.8}$	54^{+10}_{-10}	97^{+27}_{-18}	39^{+6}_{-6}	$1.0^{+0.2}_{-0.2}$	174^{+41}_{-41}	40
P20181_01	$3.5^{+0.2}_{-0.2}$	$1.1^{+0.1}_{-0.1}$	$0.73^{+0.05}_{-0.05}$	175^{+10}_{-10}	215	$6.9^{+1.5}_{-0.2}$	60^{+2}_{-11}	106^{+6}_{-26}	39^{+4}_{-6}	$0.85^{+0.08}_{-0.04}$	156^{+24}_{-13}	81
P20181_02	$3.3^{+0.4}_{-0.3}$	$1.3^{+0.2}_{-0.2}$	$0.8^{+0.1}_{-0.1}$	192^{+23}_{-23}	177	$7.7^{+0.6}_{-0.8}$	49^{+7}_{-7}	87^{+15}_{-12}	43^{+7}_{-5}	$1.0^{+0.2}_{-0.2}$	174^{+42}_{-33}	43
P20181_03	$3.6^{+0.4}_{-0.4}$	$1.2^{+0.2}_{-0.2}$	$0.8^{+0.1}_{-0.1}$	180^{+23}_{-22}	144	$8.7^{+2.5}_{-1.3}$	42^{+10}_{-41}	80^{+10}_{-18}	37^{+7}_{-4}	$0.9^{+0.2}_{-0.2}$	160^{+36}_{-41}	57
P20056_01	$3.5^{+0.4}_{-0.5}$	$1.1^{+0.3}_{-0.2}$	$0.8^{+0.2}_{-0.2}$	175^{+30}_{-29}	75	$8.1^{+2.5}_{-1.6}$	48^{+15}_{-25}	83^{+32}_{-19}	33^{+9}_{-10}	$1.0^{+0.2}_{-0.3}$	185^{+38}_{-40}	52
P20056_02	$2.8^{+0.3}_{-0.3}$	$1.2^{+0.2}_{-0.2}$	$0.8^{+0.1}_{-0.1}$	194^{+33}_{-33}	103	$6.2^{+1.5}_{-0.7}$	55^{+7}_{-12}	103^{+31}_{-25}	44^{+8}_{-6}	$1.0^{+0.2}_{-0.3}$	174^{+42}_{-47}	52
P20056_03	$2.5^{+0.3}_{-0.2}$	$1.5^{+0.1}_{-0.3}$	$0.8^{+0.1}_{-0.2}$	204^{+31}_{-34}	110	$6.1^{+1.1}_{-0.6}$	54^{+19}_{-11}	93^{+31}_{-20}	54^{+9}_{-10}	$1.3^{+0.2}_{-0.2}$	227^{+38}_{-46}	62
P20056_05	$2.0^{+0.3}_{-0.1}$	$1.5^{+0.1}_{-0.4}$	$0.9^{+0.1}_{-0.1}$	215^{+35}_{-37}	96	$7.1^{+1.5}_{-1.4}$	39^{+17}_{-14}	72^{+30}_{-14}	37^{+11}_{-8}	$1.1^{+0.2}_{-0.2}$	237^{+40}_{-44}	47
P20056_06	$2.6^{+0.3}_{-0.3}$	$1.2^{+0.3}_{-0.2}$	$0.8^{+0.1}_{-0.1}$	207^{+42}_{-38}	112	$6.0^{+1.6}_{-1.2}$	51^{+15}_{-12}	104^{+58}_{-27}	47^{+12}_{-11}	$1.0^{+0.2}_{-0.2}$	184^{+49}_{-51}	49
P20056_07	$1.9^{+0.1}_{-0.1}$	$1.5^{+0.1}_{-0.1}$	$0.8^{+0.1}_{-0.1}$	206^{+30}_{-28}	105	$5.7^{+1.1}_{-0.3}$	50^{+23}_{-11}	86^{+37}_{-16}	47^{+13}_{-8}	$0.9^{+0.2}_{-0.2}$	212^{+33}_{-39}	51
P20056_08	$1.9^{+0.1}_{-0.1}$	$1.5^{+0.1}_{-0.2}$	$0.8^{+0.1}_{-0.1}$	212^{+33}_{-31}	108	$5.5^{+1.1}_{-0.8}$	54^{+22}_{-8}	97^{+24}_{-28}	47^{+12}_{-9}	$1.0^{+0.2}_{-0.2}$	206^{+38}_{-40}	50
P20181_04	$4.4^{+0.2}_{-0.3}$	$1.1^{+0.2}_{-0.1}$	$0.7^{+0.1}_{-0.1}$	148^{+25}_{-32}	109	$8.4^{+1.6}_{-1.2}$	51^{+11}_{-12}	90^{+26}_{-17}	38^{+7}_{-7}	$0.9^{+0.2}_{-0.3}$	138^{+43}_{-39}	45
P20181_05	$7.0^{+0.1}_{-0.3}$	$1.0^{+0.1}_{-0.1}$	$0.6^{+0.2}_{-0.2}$	107^{+28}_{-26}	70	$14.2^{+1.2}_{-2.3}$	25^{+32}_{-24}	83^{+33}_{-8}	18^{+7}_{-7}	$0.3^{+0.3}_{-0.3}$	80^{+34}_{-27}	52
P20181_06	$3.9^{+0.3}_{-0.4}$	$1.3^{+0.2}_{-0.2}$	$0.7^{+0.1}_{-0.1}$	157^{+23}_{-23}	153	$9.4^{+1.4}_{-1.0}$	40^{+9}_{-21}	72^{+14}_{-8}	39^{+5}_{-7}	$0.9^{+0.2}_{-0.2}$	162^{+25}_{-33}	52
P20181_07	$2.8^{+0.2}_{-0.1}$	$1.5^{+0.1}_{-0.1}$	$0.8^{+0.1}_{-0.1}$	177^{+22}_{-22}	175	$7.5^{+1.0}_{-0.6}$	44^{+7}_{-7}	75^{+12}_{-11}	45^{+6}_{-8}	$1.0^{+0.2}_{-0.2}$	189^{+25}_{-33}	66
P20181_08	$4.4^{+0.3}_{-0.2}$	$1.1^{+0.2}_{-0.1}$	$0.7^{+0.1}_{-0.1}$	148^{+24}_{-23}	129	$9.1^{+1.6}_{-1.2}$	46^{+11}_{-12}	82^{+21}_{-15}	37^{+6}_{-7}	$0.8^{+0.3}_{-0.2}$	143^{+34}_{-33}	45
P40108_03	$1.1^{+0.1}_{-0.2}$	$1.6^{+0.4}_{-0.1}$	$0.4^{+0.1}_{-0.1}$	123^{+26}_{-23}	149	$6.8^{+0.5}_{-0.9}$	11^{+11}_{-10}	28^{+7}_{-3}	29^{+7}_{-9}	$0.8^{+0.1}_{-0.1}$	174^{+26}_{-25}	49
P40108_04	$2.8^{+0.1}_{-0.1}$	$1.5^{+0.1}_{-0.2}$	$0.4^{+0.1}_{-0.2}$	116^{+22}_{-20}	120	$10.6^{+0.3}_{-0.3}$	1^{+27}_{-0}	45^{+4}_{-3}	33^{+5}_{-6}	$0.8^{+0.2}_{-0.2}$	155^{+25}_{-23}	43
P40108_05	$3.9^{+0.2}_{-0.3}$	$1.5^{+0.0}_{-0.1}$	$0.5^{+0.2}_{-0.2}$	111^{+24}_{-23}	130	$11.7^{+0.3}_{-0.8}$	1^{+23}_{-0}	58^{+5}_{-5}	37^{+6}_{-6}	$0.8^{+0.2}_{-0.3}$	134^{+34}_{-16}	57
P40108_06	$5.1^{+0.4}_{-0.7}$	$1.4^{+0.3}_{-0.2}$	$0.4^{+0.2}_{-0.2}$	124^{+27}_{-27}	56	$13.2^{+0.7}_{-1.3}$	1^{+34}_{-0}	63^{+7}_{-7}	15^{+4}_{-5}	$0.6^{+0.2}_{-0.2}$	158^{+40}_{-38}	54
P40108_07	$3.7^{+0.6}_{-0.8}$	$0.9^{+0.5}_{-0.2}$	$0.6^{+0.3}_{-0.4}$	128^{+60}_{-63}	48	$12.2^{+0.8}_{-1.6}$	10^{+33}_{-9}	63^{+15}_{-11}	7^{+18}_{-7}	$0.6^{+0.3}_{-0.3}$	149^{+57}_{-57}	46

Table A2. Parameters for near face on *kotelp* plus dust scattering halo models fit to hard state data of GX 339–4.

Obs.	N_H (10^{21} cm^{-2})	f_{halo}	S_{halo}	ℓ_c	τ_{es}	σ_{line} (keV)	EW (eV)	χ^2/DoF	Instruments
P40108_04	6.0			$3.3^{+0.4}_{-0.2}$	$2.5^{+0.1}_{-0.1}$	$0.6^{+0.1}_{-0.1}$	169^{+28}_{-21}	94/72	<i>PCA, HEXTE</i>
	$5.1^{+0.2}_{-0.2}$	$0.40^{+0.04}_{-0.04}$	$1.8^{+0.1}_{-0.1}$	$4.0^{+0.3}_{-0.3}$	$3.6^{+0.2}_{-0.3}$	$0.7^{+0.2}_{-0.2}$	237^{+41}_{-49}	118/125	<i>GIS, SIS, HEXTE</i>
	$5.3^{+0.2}_{-0.3}$	$0.62^{+0.08}_{-0.06}$	$1.8^{+0.1}_{-0.1}$	$3.4^{+0.3}_{-0.3}$	$2.6^{+0.1}_{-0.1}$	$0.7^{+0.1}_{-0.1}$	216^{+20}_{-21}	220/172	<i>GIS, SIS, PCA, HEXTE</i>
P40108_05	6.0			$4.6^{+0.6}_{-0.3}$	$2.4^{+0.2}_{-0.3}$	$0.7^{+0.1}_{-0.2}$	158^{+28}_{-25}	105/66	<i>PCA, HEXTE</i>
	$5.5^{+0.1}_{-0.1}$	$0.49^{+0.07}_{-0.06}$	$1.7^{+0.1}_{-0.1}$	$5.9^{+0.5}_{-0.3}$	$3.0^{+0.1}_{-0.1}$	$0.7^{+0.3}_{-0.2}$	264^{+15}_{-71}	155/125	<i>GIS, SIS, HEXTE</i>
	$6.1^{+0.1}_{-0.1}$	$0.81^{+0.03}_{-0.04}$	$1.7^{+0.0}_{-0.0}$	$4.8^{+0.1}_{-0.1}$	$2.5^{+0.1}_{-0.1}$	$0.7^{+0.1}_{-0.1}$	212^{+19}_{-20}	284/166	<i>GIS, SIS, PCA, HEXTE</i>

Table A3. Parameters for the *compps* model fit to *RXTE* (*PCA*+*HEXTE*) soft state data of GX 339–4.

Obs.	kT_e (keV)	τ_{es}	kT_{dbb} (keV)	$\Omega/2\pi$ (10^{-2})	Ξ (10^4)	E_{line} (keV)	σ_{line}	EW (keV)	χ^2/DoF
P40108_01	123^{+16}_{-6}	$0.30^{+0.02}_{-0.05}$	$0.54^{+0.01}_{-0.01}$	19^{+2}_{-2}	$1.1^{+0.2}_{-0.6}$	$6.8^{+0.3}_{-0.2}$	$5.4^{+0.7}_{-0.4}$	0.6	59/67
P40108_02	136^{+8}_{-5}	$0.28^{+0.02}_{-0.01}$	$0.54^{+0.01}_{-0.01}$	20^{+2}_{-2}	$0.8^{+0.4}_{-0.3}$	$6.8^{+0.2}_{-0.2}$	$5.2^{+0.5}_{-0.4}$	0.9	68/67

Table A4. Fits to the 10–20 keV PSD of GX 339–4 (1997 hard state).

Obs.	f_{\max} (Hz)	zfc-Lor ₁	QPO ₁	QPO ₂	QPO ₃	zfc-Lor ₂	χ^2/DoF
P20181_01	20	$A = 0.13^{+0.01}_{-0.01}$ $f = 0.14^{+0.01}_{-0.02}$	$R = 0.06^{+0.01}_{-0.01}$ $f = 0.33^{+0.00}_{-0.00}$ $Q = 15^{+12}_{-4}$	$R = 0.15^{+0.01}_{-0.00}$ $f = 0.43^{+0.00}_{-0.03}$ $Q = 1.9^{+0.1}_{-0.2}$		$A = 6.7^{+0.2}_{-0.4} \times 10^{-3}$ $f = 3.7^{+0.1}_{-0.2}$	133/97
P20181_02	20	$A = 0.15^{+0.01}_{-0.01}$ $f = 0.15^{+0.01}_{-0.01}$	$R = 0.06^{+0.00}_{-0.01}$ $f = 0.31^{+0.00}_{-0.01}$ $Q = 17^{+8}_{-4}$	$R = 0.11^{+0.01}_{-0.00}$ $f = 0.42^{+0.02}_{-0.01}$ $Q = 3.5^{+0.3}_{-0.3}$	$R = 0.05^{+0.01}_{-0.01}$ $f = 0.81^{+0.06}_{-0.05}$ $Q = 3.8^{+1.3}_{-1.0}$	$A = 7.0^{+0.3}_{-0.2} \times 10^{-3}$ $f = 3.5^{+0.1}_{-0.1}$	113/94
P20181_03	15	$A = 0.15^{+0.01}_{-0.01}$ $f = 0.11^{+0.01}_{-0.01}$	$R = 0.04^{+0.01}_{-0.01}$ $f = 0.30^{+0.00}_{-0.00}$ $Q = 21^{+5}_{-5}$	$R = 0.17^{+0.01}_{-0.00}$ $f = 0.35^{+0.01}_{-0.01}$ $Q = 1.6^{+0.1}_{-0.1}$		$A = 7.1^{+0.2}_{-0.2} \times 10^{-3}$ $f = 3.4^{+0.2}_{-0.1}$	74/56
P20056_01	15	$A = 0.09^{+0.01}_{-0.02}$ $f = 0.13^{+0.02}_{-0.02}$	$R = 0.07^{+0.01}_{-0.02}$ $f = 0.37^{+0.02}_{-0.01}$ $Q = 8.1^{+2.2}_{-2.7}$	$R = 0.10^{+0.01}_{-0.03}$ $f = 0.49^{+0.05}_{-0.05}$ $Q = 1.9^{+0.5}_{-0.5}$		$A = 4.4^{+0.8}_{-0.3} \times 10^{-3}$ $f = 3.4^{+0.3}_{-0.5}$	37/52
P20056_02	15	$A = 0.06^{+0.01}_{-0.01}$ $f = 0.14^{+0.06}_{-0.03}$	$R = 0.15^{+0.01}_{-0.01}$ $f = 0.40^{+0.05}_{-0.05}$ $Q = 1.5^{+0.6}_{-0.3}$			$A = 3.5^{+0.4}_{-0.3} \times 10^{-3}$ $f = 4.0^{+0.5}_{-0.4}$	67/73
P20056_03	15	$A = 0.07^{+0.01}_{-0.02}$ $f = 0.10^{+0.03}_{-0.02}$	$R = 0.16^{+0.01}_{-0.01}$ $f = 0.40^{+0.03}_{-0.03}$ $Q = 1.5^{+0.4}_{-0.2}$			$A = 3.5^{+0.6}_{-0.3} \times 10^{-3}$ $f = 4.2^{+0.4}_{-0.4}$	54/41
P20056_05	10	$A = 0.04^{+0.01}_{-0.00}$ $f = 0.16^{+0.07}_{-0.03}$	$R = 0.13^{+0.01}_{-0.01}$ $f = 0.54^{+0.02}_{-0.04}$ $Q = 2.1^{+0.6}_{-0.5}$			$A = 2.9^{+0.3}_{-0.2} \times 10^{-3}$ $f = 4.5^{+0.6}_{-0.8}$	54/38
P20056_07	15	$A = 0.05^{+0.01}_{-0.01}$ $f = 0.17^{+0.02}_{-0.04}$	$R = 0.04^{+0.01}_{-0.01}$ $f = 0.57^{+0.02}_{-0.02}$ $Q = 18^{+13}_{-6}$	$R = 0.11^{+0.01}_{-0.00}$ $f = 0.65^{+0.03}_{-0.05}$ $Q = 2.0^{+0.4}_{-0.3}$		$A = 2.5^{+0.3}_{-0.2} \times 10^{-3}$ $f = 4.7^{+0.6}_{-0.5}$	58/70
P20056_08	10	$A = 0.04^{+0.01}_{-0.01}$ $f = 0.19^{+0.05}_{-0.02}$	$R = 0.12^{+0.01}_{-0.01}$ $f = 0.67^{+0.04}_{-0.04}$ $Q = 2.0^{+0.5}_{-0.4}$			$A = 2.1^{+0.3}_{-0.5} \times 10^{-3}$ $f = 5.1^{+1.6}_{-1.1}$	26/29
P20181_04	15	$A = 0.15^{+0.00}_{-0.01}$ $f = 0.14^{+0.01}_{-0.01}$	$R = 0.05^{+0.00}_{-0.01}$ $f = 0.34^{+0.01}_{-0.01}$ $Q = 18^{+5}_{-5}$	$R = 0.14^{+0.01}_{-0.00}$ $f = 0.42^{+0.01}_{-0.02}$ $Q = 1.7^{+0.2}_{-0.1}$		$A = 6.1^{+0.2}_{-0.2} \times 10^{-3}$ $f = 3.6^{+0.2}_{-0.2}$	78/56
P20181_05	8	$A = 0.55^{+0.13}_{-0.11}$ $f = 0.02^{+0.01}_{-0.01}$	$R = 0.26^{+0.01}_{-0.02}$ $f = 0.06^{+0.01}_{-0.00}$ $Q = 0.6^{+0.1}_{-0.0}$			$A = 13.5^{+1.4}_{-1.2} \times 10^{-3}$ $f = 2.1^{+0.2}_{-0.1}$	50/36
P20181_06	30	$A = 0.18^{+0.01}_{-0.01}$ $f = 0.09^{+0.01}_{-0.01}$	$R = 0.05^{+0.02}_{-0.01}$ $f = 0.32^{+0.01}_{-0.01}$ $Q = 13^{+9}_{-5}$	$R = 0.17^{+0.01}_{-0.01}$ $f = 0.35^{+0.01}_{-0.02}$ $Q = 1.5^{+0.2}_{-0.1}$		$A = 7.3^{+0.5}_{-0.5} \times 10^{-3}$ $f = 3.4^{+0.1}_{-0.2}$	82/64
P20181_07	30	$A = 0.14^{+0.00}_{-0.01}$ $f = 0.10^{+0.01}_{-0.00}$	$R = 0.05^{+0.00}_{-0.01}$ $f = 0.22^{+0.01}_{-0.00}$ $Q = 8.6^{+3.3}_{-2.6}$	$R = 0.08^{+0.00}_{-0.00}$ $f = 0.38^{+0.01}_{-0.00}$ $Q = 13^{+2}_{-2}$	$R = 0.15^{+0.01}_{-0.00}$ $f = 0.47^{+0.01}_{-0.01}$ $Q = 1.8^{+0.1}_{-0.1}$	$A = 6.3^{+0.2}_{-0.2} \times 10^{-3}$ $f = 3.7^{+0.1}_{-0.2}$	97/61
P20181_08	20	$A = 0.17^{+0.01}_{-0.01}$ $f = 0.11^{+0.01}_{-0.01}$	$R = 0.07^{+0.01}_{-0.01}$ $f = 0.36^{+0.02}_{-0.01}$ $Q = 4.9^{+1.6}_{-1.2}$	$R = 0.15^{+0.01}_{-0.01}$ $f = 0.41^{+0.03}_{-0.01}$ $Q = 1.3^{+0.4}_{-0.4}$		$A = 5.9^{+0.1}_{-0.1} \times 10^{-3}$ $f = 3.8^{+0.2}_{-0.3}$	64/59

Table A5. Fits to the 10–20 keV PSD of GX 339–4 (1999 hard state).

Obs.	f_{max} (Hz)	zfc-Lor ₁	QPO ₁	QPO ₂	QPO ₃	zfc-Lor ₂	χ^2/DoF
P40108_03	8	$A = 0.02^{+0.00}_{-0.00}$ $f = 0.35^{+0.05}_{-0.06}$	$R = 0.16^{+0.01}_{-0.01}$ $f = 0.96^{+0.30}_{-0.20}$ $Q = 0.7^{+0.4}_{-0.2}$				53/38
P40108_04	15	$A = 0.11^{+0.00}_{-0.01}$ $f = 0.15^{+0.01}_{-0.01}$	$R = 0.14^{+0.01}_{-0.00}$ $f = 0.55^{+0.02}_{-0.05}$ $Q = 1.8^{+0.1}_{-0.2}$			$A = 3.9^{+0.6}_{-0.2} \times 10^{-3}$ $f = 4.0^{+0.5}_{-0.3}$	110/95
P40108_05	25	$A = 0.20^{+0.01}_{-0.01}$ $f = 0.12^{+0.01}_{-0.01}$	$R = 0.07^{+0.00}_{-0.01}$ $f = 0.28^{+0.00}_{-0.01}$ $Q = 11^{+5}_{-3}$	$R = 0.09^{+0.00}_{-0.01}$ $f = 0.40^{+0.01}_{-0.00}$ $Q = 6.1^{+1.4}_{-1.0}$	$R = 0.05^{+0.00}_{-0.01}$ $f = 0.64^{+0.02}_{-0.02}$ $Q = 11^{+9}_{-3}$	$A = 9.6^{+0.4}_{-0.6} \times 10^{-3}$ $f = 2.7^{+0.1}_{-0.1}$	56/54
P40108_06	8	$A = 0.42^{+0.04}_{-0.03}$ $f = 0.05^{+0.01}_{-0.00}$	$R = 0.18^{+0.01}_{-0.02}$ $f = 0.14^{+0.02}_{-0.01}$ $Q = 1.0^{+0.2}_{-0.1}$			$A = 10.7^{+0.9}_{-0.9} \times 10^{-3}$ $f = 2.5^{+0.2}_{-0.3}$	53/36
P40108_07	5	$A = 0.43^{+0.06}_{-0.06}$ $f = 0.05^{+0.00}_{-0.01}$				$A = 8.4^{+1.9}_{-2.0} \times 10^{-3}$ $f = 1.5^{+0.6}_{-0.4}$	20/19